1   **Short title:** Portable LiDAR and 3D field phenotyping in wheat

2

3   **Large-scale field phenotyping using backpack LiDAR and CropQuant-3D to measure structural**

4   **variation in wheat**

5

6   **Authors**

7   Yulei Zhu[1+], 2018112022@njau.edu.cn

8   Gang Sun[1], 2018101176@njau.edu.cn

9   Guohui Ding[1], 2018201009@njau.edu.cn, orcid: 0000-0001-5498-6838

10   Jie Zhou[1], 2018812070@njau.edu.cn, orcid: 0000-0001-7162-4791

11   Mingxing Wen[1,2], 2017201063@njau.edu.cn

12   Shichao Jin[1], jschaon@njau.edu.cn, orcid: 0000-0003-1150-336X

13   Qiang Zhao[3], zqiang@ncgr.ac.cn, orcid: 0000-0002-8372-4463

14   Joshua Colmer[4], Josh.Colmer@earlham.ac.uk, orcid: 0000-0002-0511-685X

15   Yanfeng Ding[1], dingyf@njau.edu.cn

16   Eric S. Ober[5], Eric.Ober@niab.com, orcid: 0000-0002-4832-5897

17   Ji Zhou[1,5*], Ji.Zhou@njau.edu.cn, Ji.Zhou@NIAB.com, orcid: 0000-0002-5752-5524

18

19   [1]State Key Laboratory of Crop Genetics & Germplasm Enhancement, College of Engineering,

20   College of Agriculture, Plant Phenomics Research Center, Academy for Advanced Interdisciplinary

21   Studies, Jiangsu Collaborative Innovation Center for Modern Crop Production Co-sponsored by

22   Province and Ministry, Nanjing Agricultural University, Nanjing 210095, China; [2]Zhenjiang Institute

23   of Agricultural Science, Jurong 212400, China; [3]National Center for Gene Research, CAS Center for

24   Excellence in Molecular Plant Sciences, Chinese Academy of Sciences, Shanghai 200233, China;

25   [4]Earlham Institute, Norwich Research Park, Norwich NR4 7UH, UK; [5]Cambridge Crop Research,

26   National Institute of Agricultural Botany (NIAB), Cambridge CB3 0LE, UK

28 **Corresponding author**

29 Ji Zhou

30 Email: Ji.Zhou@NJAU.edu.cn or Ji.Zhou@NIAB.com

31

32 **One-sentence summary:**

33 CropQuant-3D and backpack LiDAR enable large-scale field phenotyping and 3D trait analysis to

34 quantify structural responses to different nitrogen treatments in wheat.

35
36 **Author contributions**

37 JZ and EO wrote the manuscript with inputs from YLZ, SCJ, QZ and JC. JZ, YLZ and GS designed

38 the 3D phenotypic analysis algorithms. YLZ, GS and JieZ implemented the software under JZ's

39 supervision. GHD and MXW performed the field wheat experiments under JZ and YFD's supervision.

40 SCJ provided LiDAR expertise. JZ, YLZ and JieZ optimised the algorithms and tested the software.

41 JZ, QZ and JC performed the data analysis. All authors read and approved the final manuscript.

42

54

55   **Abstract**

56   Plant phenomics bridges the gap between traits of agricultural importance and genomic information.

57   Limitations of current field-based phenotyping solutions include mobility, affordability, throughput,

58   accuracy, scalability and the ability to analyse big data collected. Here, we present a large-scale

59   phenotyping solution that combines a commercial backpack LiDAR device and our analytic software,

60   CropQuant-3D, which have been applied jointly to phenotype wheat (*Triticum aestivum*) and

61   associated 3D trait analysis. The use of LiDAR can acquire millions of 3D points to represent spatial

62   features of crops, and CropQuant-3D can extract meaningful traits from large, complex point clouds.

63   In a case study examining the response of wheat varieties to three different levels of nitrogen

64   fertilisation in field experiments, the combined solution differentiated significant genotype and

65   treatment effects on crop growth and structural variation in canopy, with strong correlations with

66   manual measurements. Hence, we demonstrate that this system could consistently perform 3D trait

67   analysis at a larger scale and more quickly than heretofore possible and addresses challenges in

68   mobility, throughput, and scalability. To ensure our work could reach non-expert users, we developed

69   an open-source graphical user interface for CropQuant-3D. We therefore believe that the combined

70   system is easy-to-use and could be used as a reliable research tool in multi-location phenotyping for

71   both crop research and breeding. Furthermore, together with the fast maturity of LiDAR technologies,

72   the system has the potential for further development in accuracy and affordability, contributing to the

73   resolution of the phenotyping bottleneck and exploiting available genomic resources more effectively.

74

75   **Keywords**

77

78 **Introduction**

79 With the rising world population, crop production needs to double by 2050 (UN Food & Agriculture

80 Organization, 2009). To address this growing challenge of global food security, it is important to

81 identify plants with desired traits to improve yield, resource use efficiency, quality, stress resistance

82 and adaptation, and with a smaller environmental footprint (Powlson et al., 2014; Zhang et al., 2018;

83 Swarbreck et al., 2019). Furthermore, the stability of the selected traits must be verified in the field

84 over multiple seasons and locations (Sadras and Slafer, 2012; Griffiths et al., 2015; Reynolds and

85 Langridge, 2016). For example, quantitative measurements of yield-related traits such as plant height,

86 growth rate, canopy coverage and spikes per unit area can be used to indicate and explain variations in

87 yield stability in different environments (Sadras and Richards, 2014; Valluru et al., 2017; Furbank et

88 al., 2019). In recent years, the cost of genotyping has decreased dramatically, allowing genetic

89 analysis of large populations (Cobb et al., 2013; Crain et al., 2016). However, field phenotyping on a

90 large scale under realistic field conditions remains the bottleneck in genotype-phenotype association

91 studies for crop improvement (Furbank and Tester, 2011; Yang et al., 2020). Both large-scale data

92 acquisition and analysis of multiple traits at different time points and trial locations are still

93 challenging, but often it is the meaningful phenotypic information most needed by breeders and crop

94 researchers (Fiorani and Schurr, 2013; Tardieu et al., 2017; Furbank et al., 2019).

95 To relieve this bottleneck and address challenges in field phenotyping, much attention has been

96 placed upon the applications of remote sensing, internet of things (IoT), robotics, computer vision,

97 and machine learning, resulting in a rapid technical progress in recent years (Pieruschka and Schurr,

98 2019; Zhao et al., 2019; Yang et al., 2020). A range of solutions have been developed, including the

99 use of unmanned aerial vehicles (UAVs) and manned light aircraft for studying performance-related

100 traits across fields (Bauer et al., 2019; Holman et al., 2019; Harkel et al., 2020); stationary gantry

101 systems for deep phenotyping in fixed areas (Vadez et al., 2015; Kirchgessner et al., 2017; Virlet et al.,

102 2017; Burnette et al., 2018); ground-based vehicles equipped with integrated sensor arrays to study

103 canopy-related traits (Deery et al., 2014; Barker et al., 2016; Jimenez-Berni et al., 2018); hand-held or

104 distributed sensing devices to measure various phenotypes during key growth stages (Hirafuji and

105 Yoichi, 2011; Crain et al., 2016; Zhou et al., 2017b; Reynolds et al., 2019a). These methods possess

4

106   diverse advantages and disadvantages concerning throughput, accuracy, mobility, affordability,

107   scalability and, more importantly, biological relevance (Fritsche-Neto and Borém, 2015; Furbank et

108   al., 2019; Pieruschka and Schurr, 2019; Reynolds et al., 2019b; Roitsch et al., 2019). The selection of

109   a phenotyping approach is naturally depending on the nature of the research question; but despite the

110   rapid methodological progress, gaps in large-scale field solutions remain.

111   Among recent field-based solutions, Light Detection and Ranging (LiDAR) has attracted much

112   attention as it provides information on plant morphological and structural features that are difficult or

113   costly to quantify through traditional approaches (Lin, 2015; Stovall et al., 2017). As an active remote

114   sensing technique, LiDAR computes the distance from laser scanners to a given target using pulsed

115   laser beams, through which three-dimensional (3D) geometric features of the targeted object can be

116   recorded in point cloud datasets (Arnó et al., 2013). LiDAR-based tools have been successful in

117   overcoming issues related to natural illumination and occlusion, which have been problematic for

118   many field-based methods (Sun et al., 2018; Jin et al., 2019). Although point clouds produced by

119   LiDAR can be subject to noise and imbalanced densities (Bucksch et al., 2009), recently developed

120   open-source analysis libraries such as WhiteboxTools (Lindsay, 2016) and Open3D (Zhou et al., 2018)

121   can be utilised to conduct point clouds processing. However, these libraries were developed for

122   generic 3D analysis, which requires experienced developers with a computer vision background to

123   develop tailored solutions to analyse specific LiDAR data, limiting their use by plant researchers.

124   LiDAR devices can be roughly classified into three types: airborne, fixed terrestrial and mobile

125   (Hosoi and Omasa, 2009; Lin, 2015). Plant characters that have been estimated include: crop height,

126   biomass, and canopy structure (Omasa et al., 2007; Naito et al., 2017; Harkel et al., 2020); leaf

127   number, shape, and the plant capacity to intercept solar radiation (Sun et al., 2018; Jin et al., 2019);

128   and grain yield (Jimenez-Berni et al., 2018; Li et al., 2020b). LiDAR-generated point clouds have also

129   been used to improve parameterisation of crop models, enabling *in silico* testing to optimise trait

130   combinations in breeding and crop growth simulation (Reynolds and Langridge, 2016; Wang et al.,

131   2017; Walter et al., 2019). In comparison with alternative approaches that can also record 3D plant

132   traits such as Structure from Motion (SfM) (Duan et al., 2016), time-of-flight (Paulus, 2019), micro-

133   computed tomography (Wu et al., 2019), and photogrammetry techniques (An et al., 2016; Holman et

134 al., 2016), LiDAR provides a more reliable solution in scalability and accuracy for high-throughput

135 field studies.

136 Despite these advantages, there are several problems associated with current LiDAR techniques in

137 field phenotyping. Airborne LiDAR (Li et al., 2015; Harkel et al., 2020) typically requires larger

138 multi-rotor UAVs with sufficient payload capacity (normally >5 kg), which requires special trained

139 pilot and local aviation authority's clearance, adding to hardware and operating costs. Also, big

140 drones generate strong downdraft that disrupts canopies when flying them at low altitudes to acquire

141 high-resolution imagery. Fixed terrestrial LiDAR (Omasa et al., 2007; Stovall et al., 2017; Guo et al.,

142 2018), on the other hand, is placed closer to plants and can generate high-resolution models.

143 Nevertheless, this type of system requires more time to set up, limiting its applications in large-scale

144 phenotyping. Mobile LiDAR (Arnó et al., 2013; Araus and Cairns, 2014; Deery et al., 2014; Jimenez-

145 Berni et al., 2018; Deery et al., 2020) includes handheld, backpack, and devices mounted on

146 specialised vehicles (e.g. Phenomobile), which can cover large trial areas. The main drawbacks of

147 vehicle-mounted LiDAR are the costs of purchasing hardware, operating and maintenance, as well as

148 the ability to access agricultural fields with difficult conditions or rugged terrain. Handheld LiDAR

149 devices are lightweight and easy-to-use, but usually are equipped with low-cost laser sensors, limiting

150 their capability to carry out high-quality and large-scale 3D mapping (Hyyppä et al., 2020; Jin et al.,

151 2021).

152 The backpack LiDAR (Masiero et al., 2018; Hyyppä et al., 2020; Su et al., 2020) has been applied

153 successfully to forestry studies and land surveillance in recent years, showing promise for field-based

154 crop research. Compare with other LiDAR systems, it has good mobility, relatively lightweight

155 (normally around 10 kg), and is highly integrated in hardware, which means that it is easy to operate

156 and maintain. Because the laser scanner can be used in close proximity to plants (< 3 m), it can

157 generate high-quality 3D models with up to 10 mm precision with high-end laser sensors. Depending

158 on the laser scanner equipped, backpack LiDAR system could have an effective scan range of over

159 200 m, useful for phenotyping in forestry or orchard plantations, as well as large experimental areas

160 for plants. Backpack LiDAR also provides an accurate spatial positioning system (i.e. a global

161 navigation satellite system, GNSS), customised for field mapping at walking speed to enable an

162 accurate 3D reconstruction (Masiero et al., 2018). As LiDAR technology has been maturing rapidly in

163 recent years, it is expected that costs will decrease and this type of equipment could become more

164 accessible for the research community (Guo et al., 2018; Panjvani et al., 2019; Jin et al., 2021). Still,

165 the analytic software for LiDAR-based technologies is as important as the hardware. One limitation of

166 many LiDAR-based mapping systems is the lack of widely available, open analytical software

167 solutions that can extract biologically relevant information from the large point cloud data (Lin, 2015;

168 Zhao et al., 2019; Yang et al., 2020), preventing non-expert users from taking advantage of this

169 technology for rapidly modelling crop structural features and mining phenotypic information to study

170 spatial and temporal changes (Ubbens et al., 2018; Panjvani et al., 2019; Ward et al., 2019).

171 Here, we introduce an integrated solution that combines a backpack LiDAR device with open-

172 source analytic software called CropQuant-3D for processing large-scale field phenotyping and 3D

173 trait analysis. The software employs 2D/3D image analysis algorithms and Discrete Fourier

174 Transform to derive plot-based measurements of key performance-related traits such as crop height

175 and structural variation in canopy. We developed a range of technical applications to integrate the

176 backpack LiDAR and CropQuant-3D into field-based phenotyping, including a large-scale mapping

177 protocol for cereal crops, the quick quality assessment of collected datasets at different sites, and a

178 comprehensive analysis pipeline. In a case study of wheat (*Triticum aestivum*), we describe the

179 integrated solution to quantify varietal responses to three levels of nitrogen (N) fertilisation of eleven

180 Chinese winter wheat varieties selected from the 'Zhenmai' and 'Ningmai' populations. By

181 combining 3D trait analysis and manual key yield components, we also produced a performance

182 matrix to rank and evaluate genotypic differences in N responses for the examined varieties, resulting

183 in the classification of four N response types. To ensure that our work could reach the broader

184 research community, we have developed a graphical user interface (GUI) for CropQuant-3D so that

185 non-expert users could use the software easily. Furthermore, we expanded the software package to

186 analyse point clouds generated from other sources such as gantry-mounted LiDAR and UAV-SfM

187 photogrammetry. We uploaded the CropQuant-3D software (in EXE format), executable analysis

188 source code (in Jupyter notebooks), and testing datasets to our GitHub repository, which are openly

189 available for the plant research community. Hence, we believe that the integrated solution presented

190   here is capable of addressing challenges in mobility, throughput, scalability and enabling us to analyse

191   big LiDAR-collected 3D point cloud data, which is likely to help plant researchers bridge the gap

192   between traits of agricultural importance and available genetic resources for crop improvement.

193

194   **Results**

195   *In-field mapping protocol using the backpack LiDAR*

196   Because limited research has been conducted on the use of backpack LiDAR in field phenotyping, we

197   therefore developed a range of technical applications to utilise the device in the field, including the

198   optimal distance to map cereal crops, the design of mapping routes and angles, the quick assessment

199   of the data quality, and the calibration method at different sites. For example, a grid-style mapping

200   approach was designed to routinely map the large field trial in this study (red arrows in **Fig. 1a**). We

201   first recorded the 3D geo-coordinates of the trial area using a real-time kinematic (RTK) base station,

202   which logged satellite-based positions with ± 5 mm error range in 3D (**Fig. 1b**). Then, a LiDAR

203   operator walked around the perimeter of each N treatment block in the field to map the entire

204   experiment from different angles. Due to the scan range of the LiDAR device, we did not need to

205   walk around each individual plot, saving significant time in operation. On average, it took the LiDAR

206   operator 20-25 minutes to map an experiment field of 0.5-ha, equivalent to a mapping speed of around

207   1.2 ha per hour. To study canopy structural responses to different N, we focused on the growth stages

208   between heading (GS51-59) and grain filling (GS71-89) when canopy was largely established

209   (Zadocks et al., 1974).

210

211   *Data pre-processing to generate 3D point clouds*

212   According to standard practice in processing 3D points (Kachamba et al., 2016; Duan et al., 2017;

213   Sun et al., 2018), we used the bundled pre-processing software to generate GPS-tagged 3D point

214   clouds collected by the LiDAR (**Fig. 1c**). The bundled software we used are: MMProcess to build up a

215   3D mapping project, AERO-office to define the mapping path, and GrafNav to associate RTK GPS

216   signals with the path. To select, visualise, and export point clouds, we chose to use the open-source

217 CloudCompare software (Girardeau-Montaut, 2015). The same tasks can also be accomplished by

218 using proprietary software such as TerraSolid (Korzeniowska and Łącka, 2011).

219 Because the backpack LiDAR device we used has an effective scan range of around 200 m (over

220 180 million points were collected in a single field), the mapped area (over 1.5 ha, **Fig. 1d**) was much

221 larger than the experiment region (i.e. the combined area of the 486 wheat plots, 0.5 ha). Hence, we

222 used RTK-recorded geo-coordinates to delineate regions of interest (ROI) and facilitate our routine

223 processing. After defining the ROI (over 45 million points retained for the experimental region,

224 around 90,000 points per plot), all 3D points were visualised and coloured according to their z values

225 (**Fig. 1e**). A preview of uncalibrated 3D mapping data prior to terrain adjustment enabled us to: (1)

226 associate pseudo-colour to raw 3D points for quick growth assessment; (2) perform initial

227 comparisons of experiments at multiple sites; and (3) define ROI to facilitate field- and plot-level 3D

228 points sampling.

229

230 *A comprehensive pipeline for traits analysis*

231 To carry out routine 3D points processing and trait analysis using LiDAR-collected point clouds, we

232 developed a comprehensive analysis pipeline. **Figure 2** shows a high-level workflow of the pipeline,

233 which consisted of six steps: data selection, normalisation, the generation of crop canopy height

234 model (CHM), plot segmentation, 3D trait analysis, and export of the analysis results:

235

236 1) *Step 1*: a pre-processed point cloud file (in LAS format) was selected (**Fig. 2a**). Because LiDAR-

237   collected point clouds is likely to be noisy and uncalibrated (with slopes and terrain features of the

238   field), we developed a process to normalise the 3D points (*Steps 2&3*). To remove noise, we

239   followed a published method (Su et al., 2019), which calculates the average distance between a

240   given 3D point and its neighbouring points (*avg.*). If the distance (*k*) between the point and its

241   neighbouring points (defaulted to 50) is greater than *avg.* + *k* × *std.* (where *std.* is one standard

242   deviation of the mean of all the distances), the point will be classified as an outlier. In our case, all

243   identified outliers were coloured red and removed from the following analysis (**Fig. 2b**).

244

245   *2)*   *Step 2*: after denoising, a filtering method was applied to separate ground-level and above-ground

246   3D points by applying the `LidarGroundPointFilter` function in WhiteboxTools (Lindsay,

247   2016), including (1) ground-based slope normalisation; (2) a subsequent k-nearest neighbours,

248   kNN, (Lowe, 2004) to identify neighbouring points within a defined *radius* (defaulted to 2) to

249   examine height differences; and (3) a classification method to classify ground-level and above-

250   ground points. The use of the function resulted in a flattened ground plane, enabling precise

251   measurements of above-ground 3D points. The output of *Step 2* is saved in a new LAS file with

252   all the ground-level points assigned with *zero* z-values (dark blue) and above-ground points

253   assigned with height values in centimetre (cm).

254

255   *3)*   *Step 3*: a key step in the pipeline used to generate a CHM for 3D trait analysis. First, because the

256   density of LiDAR-collected point clouds is likely to be unbalanced (e.g. denser 3D points for

257   objects close to the laser scanner, **Fig. 1d**), we improved a progressive triangulated irregular

258   network (TIN) algorithm (Zhao et al., 2016) to interpolate the unbalanced point clouds. Then, we

259   utilised all the filtered above-ground points to generate a digital surface model (DSM), followed

260   by the conversion of geo-coordinates on the x and y axes into pixel coordinates (Ritter and Ruth,

261   1997) to define four ROI markers in the DSM (**Fig. 2c**). When processing a series of point cloud

262   files collected from the same field, these four markers could be used repeatedly. To reduce

263   computational complexity, we associated z values of each 3D point with a grayscale value (i.e. 0

264   cm is taken to be black, and 160 cm is taken to be white; the taller the point, the higher the

265   grayscale value), followed by a projection method to cast all 3D points onto the flattened ground

266   plane. This process produced a 2D CHM image from an overhead perspective (**Fig. 2c**). Finally,

267   we performed a 2D perspective transform (Mezirow, 1978) using the

268   `getPerspectiveTransform` function in OpenCV (Howse, 2013) to extract the region within

269   the four markers and then align the CHM for automated trait analysis. The 2D CHM image

270   contains spatial information of all the plots in the experimental field.

271

272   *4)* *Step 4*: to segment plots using the 2D CHM, we employed the 2D Hough transform (Duda and

273   Hart, 1972) to detect plot boundaries. Because the gap between plots could be unclear during the

274   season (e.g. lodging could cover the gap), missing pixels between plots or noise could affect the

275   result of the Hough transform. Hence, we designed an improved method to detect horizontal and

276   vertical lines separately (**Fig. 2d**), including: (*Step 4.1*) combining both global (Sauvola and

277   Pietikäinen, 2000) and local thresholding (Firdousi and Parveen, 2014) methods to establish an

278   initial plot mask for the CHM, even if the background is not uniform; (*Step 4.2*) using the *Sobel*

279   operator (Kroon, 2009) to detect the horizontal and vertical edges (angles were set at 360 and 30

280   as all the CHMs were aligned); (*Step 4.3*) drawing straight lines based on the detected edges (with

281   right angles, x- and y-intercept as input parameters) using the `hough_line` and `line_aa`

282   functions in Scikit-Image (van der Walt et al., 2014); (*Step 4.4*) merging multiple detected lines if

283   they were close to each other, so that only a single line could represent the gap between plots

284   (**Fig. 2e**). Finally, assembling the lines and producing a final plot-level mask to present all of the

285   plots in the field (e.g. 162 plots in **Fig. 2e**). To remove edge effects, gaps within plots due to plant

286   sampling, and crop variation that is not directly linked to the varieties or treatments (e.g. N loss),

287   we calculated the weighted centroid of each plot using grayscale-based entropy features (Susan

288   and Hanmandlu, 2013) within a given plot . Through this approach, width and length of a plot

289   mask could be adjusted adaptively to rectify the plot-level sampling areas.

290

291   *5)* *Steps 5&6*: the last two steps of the pipeline measured and exported key performance- and yield-

292   related traits for each plot. A range of traits have been measured, including crop height, 3D

293   canopy uniformity, 3D canopy surface, canopy coverage and biomass estimation (i.e. 3DVI and

294   3DPI). A table (in CSV format) was generated and populated with these scores, with each row

295   corresponding to a plot (i.e. a variety) and each column corresponding to a trait, arranged

296   according to the plot location (i.e. row and column IDs) in the field (**Fig. 2f**).

297

298 *The GUI of CropQuant-3D*

299 To facilitate non-expert users to process 3D point clouds (in LAS format), we developed the GUI of

300 CropQuant-3D, which integrated the above analysis pipeline into a single dialogue panel, from which

301 all the above algorithmic steps could be performed. The GUI was implemented using PyQt5, a

302 comprehensive set of Python bindings for the Qt v5 library (Summerfield, 2015), allowing the GUI to

303 be executable on varied operating systems (see **Availability and requirements**). Following a similar

304 systems design described previously (Zhou et al., 2017a), CropQuant-3D uses a stepwise approach to

305 process point clouds and analyse 3D traits. The initial window (**Fig. 3a**) shows several sections with

306 default input parameters pre-populated. In the input section, a user needs to select a LiDAR file (test

307 LAS files provided on the GitHub). Then, the user needs to pre-process the selected point cloud file,

308 including denoising and ground-based filtering (*Steps 1 & 2* in the GUI). After pre-processing, the

309 user can generate a 2D CHM (*Step 3*) by defining the exchange rate between a pixel and a metric unit

310 (i.e. cm), followed by defining geo-coordinates of the experimental field (i.e. ROI markers; *Step 4*).

311 The *Step 5* is to segment plots using the 2D CHM, so that traits such as plot-based height and canopy

312 coverage can be measured (*Step 6*). Finally, if the user needs to export point clouds for specific plots,

313 the user can click four corners of one or multiple plots in the CHM following the order, upper-left,

314 upper-right, lower-left and lower-right (*Step 7*, optional). To enable a fast selection of plot-level 3D

315 points, we used the `EVENT_LBUTTONDOWN` function in OpenCV to create a mouse response event.

316 The analysis results can be downloaded after all the mandatory steps are accomplished (**Fig. 3b**).

317   When a step is finished, a green-coloured message will be displayed in the section together with a

318 Display button to show intermediate results (**Fig. 3c**). In particular, if the plot boundaries are unclear

319 and the plot segmentation algorithm fails to segment all the plots, the user can define the field layout

320 (i.e. the number of rows and columns) through an optional input box, which will generate base lines to

321 assist the plot segmentation. Furthermore, to enable the GUI software to process point clouds

322 produced from other sources such as UAV-SfM photogrammetry and LiDAR mounted on gantry

323 systems, we expanded the input function to accept these types of point cloud files (in LAS format).

324 For example, the CropQuant-3D GUI can process point clouds generated by both UAVs (**Fig. 3d**) and

325 FieldScan^TM (Phenospex, Netherlands; **Fig. 3e**) through unified analysis steps in the software to

326 perform plot-based 3D trait analysis. A detailed step-by-step user guide (**Supplemental Methods S1**)

327 and an instructional video (**Supplemental Movie S1**) for the GUI-based software can be seen in the

328 **Supplemental Data**. The software implementation can be seen in the **Materials and Methods**

329 section.

330

331 *Height measurement using CropQuant-3D*

332 Plant height and the rate of height increase (i.e. growth rate) are important performance- and yield-

333 related traits (Holman et al., 2016; Nguyen and Kant, 2018; Momen et al., 2019). For field-based

334 phenotyping, we found that, although terrain adjustment (e.g. slope removing) is a standard process

335 for height estimates from elevation models in large-scale land surveillance and forestry research, there

336 are no standardised approaches designed for such adjustment in relatively small-scale crop fields.

337 Hence, we have implemented a customised solution to normalise slopes and terrain features before

338 height mapping. To measure crop height in a given plot, our algorithm was partially based on

339 a mobile laser scanning approach described previously (Friedli et al., 2016), but performed on a

340 flattened ground plane (*Steps 3&4* in the pipeline) with the highest 10% 3D points (H_{10}) sampled in

341 the plot to reduce height variances at the canopy level. The average height value of the H_{10} set was

342 computed as the plot-level crop height. We produced three sets of height maps for all the six-metre

343 486 plots under three N treatments at the heading stage, with a unified height scale bar (**Fig. 4**). The

344 3D DSM and 2D CHM images (**Fig. 4a-c**, left) show the 3D reconstruction and height distribution of

345 the three N blocks, from 60-degree and overhead perspectives; whereas the coloured height maps (**Fig.**

346 **4a-c**, right) demonstrate how height of wheat plants responded to different levels of N treatments

347 (**Supplemental Table S1**).

348

349 *3D Canopy surface and canopy coverage measures*

350 The rates of carbon gain through photosynthesis and water loss through transpiration of the canopy

351 can be affected by changes in canopy structure, which can be used to explain crop performance and

352 plants' responses to environment (Green et al., 1985; Shearman et al., 2005). However, it is

353 challenging to measure canopy structural characters due to its complexity and dynamic spatial

354 variability caused by genetic, agronomic management, and environmental effects (Omasa et al., 2007;

355 Hosoi and Omasa, 2009; Duan et al., 2016). Although LiDAR devices have been used to visualise 3D

356 canopy structure, how to quantify structural changes using point clouds was still a challenge that

357 needed to be addressed.

358 We approached the matter through measuring a range of traits at the canopy level, including 3D

359 canopy surface area and canopy coverage. To measure canopy coverage index, we developed the

360 following steps: (1) retaining highest 50% 3D points (H_{50}) in a given plot (**Fig. 5a**); (2) then,

361 projecting H_{50} points onto a flattened plane to generate a 2D canopy image from an overhead

362 perspective; (3) after that, applying the `threshold_local` function in Scikit-Image (Singh et al.,

363 2012) to select pixels in the canopy image using the calculated local threshold, resulting in a binarized

364 canopy mask to represent the canopy coverage in a plot. We applied the trait to measure the canopy

365 coverage differences of a wheat variety (e.g. NMzi-1019) under three N treatments. The canopy

366 coverage index (0-1, where 1 is 100% coverage) showed an increase of 10-15% when the N

367 fertilisation increased (**Fig. 5b**).

368 While the canopy coverage is important as it relates to the interception of direct solar radiation, it

369 does not account for the total leaf area of the canopy, which is a more precise measure of interception

370 of diffuse radiation and reflected light within the canopy (Cabrera-Bosquet et al., 2016). As the 3D

371 surface area of the canopy would be closely related to the total transpirational leaf area and would

372 correspond with the summed photosynthetic activity of all leaves (Omasa et al., 2007), we therefore

373 included the measurement of 3D canopy surface area in the CropQuant-3D (**Fig. 5c**). The algorithmic

374 steps were designed based on the triangle mesh method (Edelsbrunner et al., 1983), including: (1)

375 applying the voxelization method (Truong-Hong et al., 2013) to generate a 3D grid system to package

376 all the above-ground 3D points into voxels; (2) using the `voxel_down_sample` function from

377 Open3D to down-sample the number of voxels, so that gaps between plants in a given plot could be

378 covered; (3) using the `create_from_point_cloud_alpha_shape` function (Edelsbrunner et al.,

379 1983) to reconstruct 3D surfaces of the canopy, followed by the `get_surface_area` function to

380 calculate the 3D surface area. For example, the 3D surface area indices of wheat variety NMzi-1019

381   showed an increase of over 20% with the increase in N application levels (**Fig. 5d**). In addition to the

382   above two traits, we also integrated traits such as 3D voxel index (3DVI) and 3D profile index (3DPI)

383   into CropQuant-3D to estimate biomass, which has been described previously (Jimenez-Berni et al.,

384   2018; Deery et al., 2020). All the above trait analysis results are listed in **Supplemental Table S2**.

385

386   *An original canopy structural measure – 3D canopy index*

387   Whilst the above indices are useful measures to describe some canopy structural features, they do not

388   convey information about canopy-level changes in spatial characteristics (e.g. height variation) across

389   the plot, which are likely to be affected by many factors in the field experiments, including: (1) plant

390   architecture such as individual tillers (e.g. main stem is taller than secondary tillers), which could

391   differ between genotypes; (2) the height of spikes if a mixed population was drilled; (3) the density of

392   the crop (e.g. spikes number per unit area, $SN\ m^{-2}$) due to different management practices such as the

393   seeding rate, (4) agronomic or environmental reasons unrelated to treatment or genotype (e.g. local

394   seedbed variations), and (5) lodging. We have established an original algorithm incorporated in the

395   CropQuant-3D software to measure spatial differences at the canopy level. Following the previous

396   naming convention (Jimenez-Berni et al., 2018), we called this measure 3D canopy index (3DCI). The

397   algorithm for 3DCI consists of five key steps:

398

399   1) Using the plot-level masks (**Fig. 2e**), we extracted all the above-ground 3D points in a given plot

400   to generate a pseudo-colour spatial map from an overhead view. We then transformed the map

401   into a grayscale image with each pixel's grayscale value corresponding to its height value,

402   resulting in a 2D plot-level CHM (**Fig. 6a**, right).

403

404   2) A 2D discrete Fourier Transform (DFT) method (Cooley and Tukey, 1965) was applied to

405   represent the plot-level CHM in the frequency domain, producing the magnitude of the image's

406   Fourier transform. Because the dynamic range of the Fourier coefficients was too large to be

407   visualised, we applied a logarithmic transform and generated a frequency spectrogram (**Fig. 6b**),

408   containing all frequencies of the spatial information in the plot and their magnitude. The DFT can

409   be defined as:

410    $$f(x, y) = \frac{1}{MN} \sum_{u=0}^{M-1} \sum_{v=0}^{N-1} F(u, v) e^{j2\pi(\frac{ux}{M} + \frac{vy}{N})}; \; x = [0, M-1], y = [0, N-1] \qquad (1)$$

411   Where *f(x, y)* represents the M×N spatial domain matrix, and *F(u, v)* represents the DFT of *f(x,*

412   *y)*. The coordinate system of *F(u, v)* is in the frequency domain.

413

414   3) We centralised the frequency spectrogram to remove periodic interference signals, resulting in a

415   centralised magnitude image to represent the spatial information. For example, by applying DFT

416   to CHM images under three N treatments, we could identify different structural features at the

417   canopy level (**Fig. 6c**): (a) the magnitude of the low-N magnitude image became rapidly smaller

418   for higher grayscale values (e.g. canopy objects such as wheat spikes), suggesting its canopy was

419   lower and the distribution of its spatial features was spread out (i.e. less dense) compared with

420   crops under medium or high N treatments; (b) the main values of spectrogram images for both

421   medium and high N applications lay on a vertical line, suggesting their canopy structures

422   contained a dominating vertical orientation caused by regular patterns (e.g. lines formed by

423   plants); and (c) in the medium-N magnitude image, another pattern could be observed which

424   passed through the center at 75-80° angle (highlighted by a light-green dashed oval), which was

425   caused by another spatial pattern in the plot and potentially could be a useful tool to measure the

426   degree of lodging (**Fig. 6a**).

427

428   4) To utilise the above DFT results in quantitative trait measurements, we sampled all the pixels'

429   grayscale values on the diagonal of the centralised magnitude image (red coloured lines in **Fig.**

430   **6c**), based on which frequencies of all spatial values and their amplitude were summarised. We

431   then used the Gaussian fitting to plot the amplitude of the sampled spatial values, producing

432   curves to represent canopy structural features within a defined frequency region, where the x-axis

433   denotes frequencies of canopy-level spatial values, and the y-axis represents their associated

434   amplitude (**Fig. 6d**). Two important features could be concluded from canopy structural curves:

16

435   (a) the curvature of these curves, signifying the density of crop canopy, as a less dense canopy

436   structure contained larger spatial variation (e.g. less dense spikes) and resulted in a higher

437   curvature ; (b) the area beneath the structural curve (e.g. with light red diagonal stripes, **Fig. 6d**),

438   showing the canopy uniformity – when curvatures are similar, structural curves comprise greater

439   area indicates less uniformity due to greater accumulated spatial variances. We used integral

440   calculus (i.e. integration) to compute the area beneath the canopy structural curve, which is

441   defined by Eq.2:

442    $$\int_a^b f(x)d(x) \approx \sum_{k=1}^N \frac{f(x_{k+1})+f(x_k)}{2}\Delta x_k; \ x \in [a,b], k = [1,N] \tag{2}$$

443   Where x is frequencies of spatial values, a is the minimum frequencies of spatial values (set

444   as -100), b is the maximum frequencies (set as 100), $f(x)$ is the amplitude value after

445   Gaussian fitting, N is the total number of x sampled, Δx_k is the difference between x_k and

446   x_{k+1}.

447

448   To compute the curvature of a structural curve, we used Eq. 3 as described previously (Van Der

449   Walt et al., 2011):

450    $$Curvature = (|\frac{d^2x}{dt^2} * \frac{dy}{dt} - \frac{dx}{dt} * \frac{d^2y}{dt^2}|)/(\frac{dx}{dt} * \frac{dx}{dt} + \frac{dy}{dt} * \frac{dy}{dt})^{3/2} \tag{3}$$

451   Where x represents the frequency array (the x-axis), y is the amplitude array (the y-axis).

452

453   5) To use the above equations for measuring canopy uniformity, we normalised values generated by

454   Eq2., so that we could cross-validate the measure for different varieties. We called this

455   normalised value 3DCI. The normalisation is defined by Eq4.:

456    $$y = \frac{x-MinValue}{MaxValue-MinValue} \tag{4}$$

457   Where x is the calculated value using Eq2., y is the normalised 3D canopy uniformity index,

458   *MinValue* is the theoretical minimum value from the value list, i.e. 59.3% of the calculated

459   minimum value (Raybould and Quemada, 2010); and *MaxValue* is the theoretical maximum

460   value from the value list, i.e. 129.4% of the calculated maximum value.

17

461

462   To verify the 3DCI and curvature measures, we used the wheat variety NMzi-1019, which has

463   shown to respond strongly to different levels of N fertilisation (Feng et al., 2008). Three canopy

464   structural curves of NMzi-1019 under three N treatments (n = 9 plots) were produced (**Fig. 6d**). The

465   three curves' curvatures reduced moderately when the N fertilisation increased, indicating the canopy

466   density were increasing. The high-N canopy curve (coloured red; 3DCI = 0.471) contained less

467   accumulative spatial variation than those with low (coloured blue; 3DCI = 0.554) and medium-N

468   (coloured light green; 3DCI = 0.513) treatments (see cross sections in **Fig. 6d**) and hence possessed a

469   smaller area beneath the curve. Trends in 3DCI scores across N treatments could also be used to

470   differentiate varietal differences in canopy responses to N treatments. For example, increasing 3DCI

471   indicated that the canopy became more variable in height, suggesting more structural responses to N

472   applications. Similarly, if the index decreased sharply with the N increase, this indicated that the crop

473   canopy became more uniform rapidly and likely much denser when the N application changed.

474

475   *Validation of the CropQuant-measured traits using ground truth data*

476   Height estimates derived from the CropQuant-3D output were validated by comparisons with manual

477   height measurements taken at the same stage of crop development (grain filling) in the 2019/20 trial.

478   There was a strong correlation between the CropQuant-3D's height scores and manual measurements

479   for each level of N, using plot-based (the square of the correlation coefficient, R^2, ranges from 0.69

480   and 0.87; *p*-value in linear regression analysis is less than 0.001; **Fig. 7a**; **Supplemental Table S3**)

481   and variety-based means (R^2 ranges from 0.84 and 0.92, $p < 0.05$; **Fig. 7b**; **Supplemental Table S4**).

482   Thus, the CropQuant-3D height scores based on the backpack LiDAR provides a viable alternative to

483   manual height measurements, particularly for obtaining genotypic means. It is interesting that

484   CropQuant-3D tended to underestimate the height for wheat varieties that are taller than 90 cm (some

485   landraces were included). This is likely due to the way manual measurements were taken, which

486   involved lifting and straightening curved or lodged plants to measure the distance from the soil

487   surface to the tip of the ear along the vertical stem, whereas the LiDAR system measured the plants as

488   they were naturally in the field. Furthermore, because only a limited number of plants were measured

489 in each plot manually, compared with a whole plot scan conducted with the backpack LiDAR, there is

490 greater chance of plot-to-plot variability with the manual approach than with LiDAR, which integrates

491 height measurements over a larger number of plants in a plot. Also, better variety-based correlation

492 values might be due to height values for each variety have been averaged (three replicates per variety),

493 reducing the height variance caused by treatments and small agronomic differences.

494   To verify the biological relevance of the 3D canopy surface area index, we have analysed

495 correlations with plot-level grain number (GN m^{-2}) and grain yield (GW m^{-2}) using data collected

496 from the 11 selected varieties (n = 81 plots). Strong positive correlations between this LiDAR-derived

497 trait and the yield components, with R^2 ranging from 0.71 to 0.76 ($p < 0.001$, **Fig. 7c**; **Supplemental**

498 **Table S5**), suggest a mechanistic link between the canopy trait and grain formation underlying the

499 correlation, indicating that the 3D surface area index can serve as a good predictor of dynamic varietal

500 performance. Additionally, there was a strong negative correlation between 3DCI (designed to

501 quantify canopy uniformity and density) and manual measured spike density (SN m^{-2}) trait, with R^2

502 ranging from 0.77 to 0.81 ($p < 0.001$, **Fig. 7d**; **Supplemental Table S6**). Hence, it is likely that the

503 3DCI could also be used as a measure to quantify how SN m^{-2}, a key yield component, responds to

504 different N applications, but without the slow and laborious process of manually counting spikes in

505 the field.

506

507 *A case study of classifying nitrogen responses for wheat*

508 To effectively select crop varieties with an improved N response (e.g. high nitrogen use efficiency,

509 NUE), it would be valuable to make use of proxy traits that are related to NUE under field conditions

510 (Sylvester-Bradley and Kindred, 2009; Pask et al., 2012; Nguyen and Kant, 2018). The range of

511 variables (e.g. 3D canopy surface area, canopy coverage, plot height and 3DCI) measured by

512 CropQuant-3D were used jointly to describe canopy structural responses to three N treatments, which

513 have enabled us to classify the N response of 11 selected wheat varieties (81 plots) into four classes

514 (**Fig. 8**). The example varieties were as follows:

515

516   1) Class 1 – canopy structural curves differed across all three N levels. The patterns for ZM-4 could

517   be clearly separated under the three N treatments (**Fig. 8a**), indicating that this type of wheat

518   variety had a strong structural response to varied N applications at the canopy. Both 3DCI

519   (coloured according to their associated N treatments) and the curvatures of the three canopy

520   curves reduced steadily together with the increase of N, indicating that spike density and canopy

521   uniformity were both rising in response to the escalation of N treatment. Also, the decrease of

522   3DCI corresponded with a continual increase of the SN m^{-2} reading. Other lines from the 11

523   varieties that can be categorised into Class 1 are NMzi-1019, ZM-5 and ZM-11 (**Supplemental**

524   **Figures S1**).

525

526   2) Class 2 – canopy structural curves were similar at low and medium N levels, but differed at high

527   N. The patterns for NMzi-1 showed that the line had a good response to increased N, but only

528   above the medium rate of N fertilisation. Both 3DCI and SN m^{-2} suggested that low and medium

529   N had similar effects on the variety (**Fig. 8b**). The SN m^{-2} scores increased distinctly only under

530   high N. Other lines that can be categorised into Class 2 are ZM-10 and ZM-12 (**Supplemental**

531   **Figures S2**).

532

533   3) Class 3 – canopy structural curves were similar at medium and high N levels. The patterns for

534   NM-8 suggested that the variety had similar responses under medium and high N treatments,

535   indicating the increasing N fertilisation was not able to increase the line's spike density beyond

536   the medium rate of N fertilisation (**Fig. 8c**). The other line that can also be categorised into Class

537   3 is ZM-26 (**Supplemental Figures S3**).

538

539   4) Class 4 – canopy structural curves decreased at high levels of N and showed the best response at

540   medium N. Curvature patterns of ZM-168 indicated that the line had a similar canopy density at

541   medium and high N treatments. The canopy uniformity was greater at the medium N level (3DCI

542   = 0.506; **Fig. 8d**) and the line's spike density was the highest among the three N treatments. The

543   other line that can be categorised into Class 4 is ZM-09196 (**Supplemental Figures S4**).

544

545 After classify N response patterns, we then combined 3DCI, crop height, canopy surface index

546 area with the yield components, GN m^{-2} and SN m^{-2}, to produce a performance matrix to understand

547 crop responses to different N treatments in a compound manner. In the matrix, each variety was

548 ranked based on the performance of these measures and traits. For example, by calculating the

549 deviation of them based on the trimmed mean values (i.e. 15% over the trimmed mean coloured dark

550 orange and placed in rank order 5, the highest rank; 7.5~15% coloured light orange and placed in rank

551 4; -7.5~7.5% coloured yellow and placed in rank 3; -15~-7.5% coloured light blue and placed in rank

552 2; and -15% below the trimmed mean coloured dark blue and placed in rank 1, the lowest rank), we

553 could select lines with a desired performance under the three N treatments using a ranking system. In

554 particular, for crop height, both very short and very tall were ranked undesirable (i.e. placed in rank 1),

555 whereas both GN m^{-2} and SN m^{-2} were given more weight (Langer and Liew, 1973) than other

556 measures ($weights = [0.25, 0.25, 0.2, 0.1, 0.2]$). Through the ranking system, we concluded that: (1)

557 for the low N treatment, ZM-168 achieved a more balanced score in terms of grain production and

558 structural variation (**Fig. 9a**); for the medium N application, NM-26 ranked the highest (**Fig. 9b**); and,

559 for the high N, NM-26 was scored the highest (**Fig. 9c**). Although this is only an initial attempt for

560 selecting wheat varieties with desirable N responses using LiDAR-derived traits and key yield

561 components, it is evident that the performance matrix could provide an objective approach to rank

562 multiple wheat varieties. Further validation and field studies using the above approach are ongoing

563 and will be reported separately.

564

565 **Discussion**

566 Plant phenomics is an important area that helps provide valuable phenotypic information that is

567 needed to fully exploit available genomic resources. For crop improvement programmes, the focus is

568 on multi-location and large-scale field phenotyping, yet there are a number of weaknesses with

569 current solutions (Tardieu et al., 2017; Furbank et al., 2019; Pieruschka and Schurr, 2019), concerning:

570 (1) mobility (a method can be straightforwardly used in multiple locations); (2) affordability (whether

571   purchase, operation and maintenance of a system can be afforded by research groups with acceptable

572   resources); (3) throughput (the number of plots, traits and fields that can be measured within a

573   reasonable time frame, as well as the number of times to phenotype in a growing season); (4)

574   accuracy (the information truly relates to the target attributes or biological functions of the plant); (5)

575   resolution (if the method provides information at the level of detail required to test the biological

576   hypothesis); and (6) scalability (the size of trials that can be phenotyped and the number of locations

577   that can be covered).

578   In addition to data collection, another issue that limits the use of field phenotyping tools involve the

579   ability to analyse big data acquired from the field (Kelly et al., 2016; Scharr et al., 2016; Cendrero-

580   Mateo et al., 2017; Lobet, 2017). Although many open-source and proprietary software solutions have

581   been developed (Butler et al., 2020; Roussel et al., 2020), their applications are normally limited to

582   certain devices and for specific research questions, leading to matters such as software usability, data

583   interoperability, and the generalisability (Carpenter et al., 2012; Roitsch et al., 2019). To address

584   some of the above issues, we pioneered the integration of backpack LiDAR and an open-source

585   software implementation to measure genotypic and N treatment differences in spatial features in

586   wheat. Results from field experiments showed that structural measures (e.g. height, 3DCI, and canopy

587   surface area) are highly correlated with key yield components such as SN m^{-2} and GN m^{-2}, indicating

588   the system could be used as a reliable research tool to classify the plant responses to different N

589   treatments.

590

591   *The backpack LiDAR hardware*

592   We have shown that the backpack LiDAR device introduced here is integrated and portable, enabling

593   the collection of high-density 3D point clouds at the field and plot levels. Typically, these kinds of

594   data would require LiDAR systems to be mounted on a gantry or vehicle platform, which are often

595   not available, too costly, fixed in one location, or cannot reach fields with limited accessibility. To our

596   knowledge, the backpack LiDAR system has not been used in field-based plant phenotyping

597   previously. Hence, we developed a range of techniques to apply the device in wheat field experiments.

598   Our field testing and development experience show that the backpack LiDAR possesses three notable

599   features: (1) large-scale capability (up to 210 m effective scan range through our equipment), with an

600   acceptable mapping speed (up to 1.2 ha per hour); (2) portability (the ability to conduct multi-location

601   phenotyping) with limited adjustments of hardware and software; (3) relatively small operation and

602   maintenance costs due to its integration, ease-of-use and mobile features. Hence, backpack LiDAR

603   appears to provide a more balanced solution to some current phenotyping challenges. Although

604   backpack LiDAR, like most high-resolution LiDAR systems with high-end scanners, is still relatively

605   expensive. However, costs should decrease and become more affordable as the technology matures

606   (Su et al., 2020). Comparisons between backpack LiDAR devices and other approaches can be seen in

607   the section below.

608

609   *CropQuant-3D software and trait analysis*

610   Processing of 3D point cloud data collected by LiDAR systems for 3D trait analysis is still

611   complicated and computationally demanding, indicating the necessity of reliable analytic solutions.

612   Furthermore, for solutions that can be used by non-experts and widely accessible by the plant research

613   community, the software should be user-friendly and openly available. Therefore, we developed the

614   CropQuant-3D analysis software to routinely process large point cloud datasets. To help other

615   researchers exploit our analysis algorithms integrated in the software, besides the GUI software, we

616   also modularised the analysis tasks into individual procedures and then saved them with executable

617   Python source code in Jupyter notebooks that can be executed on multiple operating systems. The

618   algorithmic steps include pre-processing of 3D point clouds (**Supplemental Methods S2**), automated

619   plot segmentation with optional experimental layout input, and plot-level crop height (see

620   **Supplemental Methods S3**), 3D trait analysis of canopy structural features (3DCI, 2D canopy

621   coverage, 3D canopy surface area), and biomass estimation such as 3DVI and 3DPI (see

622   **Supplemental Methods S4**). Compared with previously work (Ward et al., 2019; Hyyppä et al., 2020;

623   Su et al., 2020), we have made progress in several areas for large-scale 3D trait analysis in plants:

624

625   1)   Due to the huge volume of raw point cloud data collected, efficient data processing needs to be

626   considered for both throughput and accuracy. Many existing methods require much computational

627   time to pre-process point clouds. In our case, we have chosen to use a ground-level filter with

628   parameters tailored for small-scale crop field, retaining only 3D points required by trait analysis.

629   This approach noticeably reduced processing time. For example, for a 400 MB LiDAR file (over

630   15 million 3D points), only 100-120 seconds were required to normalise 3D points on an ordinary

631   computer (intel i7 CPU and 16 MB memory; see profiling in the **Material and Methods**).

632

633   2)   We analysed plot-level 3D traits using 2D CHM, which retains sufficient spatial information in

634   2D pixels. This approach enabled us to employ computationally more efficient 2D-based

635   algorithms such as edge detection, Hough transform, and adaptive thresholding to perform plot

636   segmentation and trait analysis, reducing the computational complexity. Another key benefit for

637   this 3D-to-2D transformation is that analysis regions could be controlled dynamically in any plot

638   region. By calculating the texture entropy (Haralick et al., 1973), we could compute the weighted

639   centroid of a plot and then define the sampling area according to experimental needs.

640

641   3)   Since the density of the LiDAR-collected 3D points is likely to be imbalanced (e.g. the further

642   away from the mapping route, the sparser the 3D points), it is necessary to interpolate the point

643   clouds if the number of 3D points in a given plot is limited. From a range of interpolation

644   algorithms, we have chosen the progressive TIN to build a TIN-based model and then densify 3D

645   points in an iterative manner, which helped us improve the quality of 3D trait analysis while

646   retaining key 3D geometric features at the plot level.

647

648   4)   It is technically difficult to describe 3D canopy structure in a quantitative manner. The 2D Fourier

649   transform method employed by CropQuant-3D opens a door to quantify spatial variances, spike

650   density and uniformity at the canopy level by dividing frequency and amplitude of all height

651   values across the plot. A similar idea but with a different approach can be found in measuring the

652   canopy roughness of leafy trees in forest ecology (Antonarakis et al., 2010). Our approach was

653   able to show that, through the canopy structural curve and 3DCI (**Fig. 6d**), we could quantify the

654   uniformity and density of wheat spikes in plots, which could be used to classify varieties

655   according to different responses to N treatments and potentially other treatments. Meanwhile, the

656   curvature of the canopy curves can also be employed to help distinguish the canopy density in

657   relation to different N treatments and varieties.

658

659   There are many vision-based approaches developed to mine spatial and temporal features from point

660   clouds for a range of biological questions, for example, identifying phenotypic differences at the

661   organ level (Li et al., 2020a) and the extraction of single plants within a plot (Jin et al., 2021).

662   Because our research aim was to enable large-scale field phenotyping for plot-level 3D trait analysis,

663   we therefore did not consider plant-level 3D reconstruction and methods to analyse detailed features

664   (e.g. plant-level marching cubes, leaf curvature estimation, and 3D skeletonization) in this work.

665

666   *Wheat varietal responses to different nitrogen fertilisation levels*

667   NUE in crops is generally low. Approximately 40% of the applied N can be utilised by cereal crops,

668   with the bulk of the remainder leaching to groundwater or volatilising to the atmosphere, causing

669   increased agricultural costs and negative impacts on the environment (Raun and Johnson, 1999; Good

670   et al., 2004). Breeding crop varieties with improved NUE should contribute to more sustainable

671   cropping systems. To effectively select lines with heritable NUE-related proxy traits under different

672   field conditions, it is technically difficult to screen many complex traits due to their dynamics and

673   complexity (Good et al., 2004; Sylvester-Bradley and Kindred, 2009).

674   In the case study, we have explored a comprehensive procedure to quantify N responses of different

675   wheat varieties based on phenotypic traits and key yield components. When the level of N changed,

676   different varieties varied with their responses in terms of canopy structural features and key yield

677   components. By combining key yield components and LiDAR-derived trait values, we identified four

678   NUE types using the subset of 11 varieties: (1) grain yield responded well to increased N applications

679   (Class 1); (2) only higher N was able to increase yield (Class 2); (3) medium and high N treatments

680   led to similar grain production (Class 3); and (4) higher N led to a yield decrease (Class 4). We

681   believe that the combined performance matrix demonstrated in the case study is likely to help

682   establish an objective approach to identify wheat lines with superior N responses, which may lead to

683   an effective selection improvement of NUE in wheat breeding programmes in the future. Further work

684   to link this selection approach with yield production and NUE at a large scale is ongoing.

685

686   *Applications of CropQuant-3D*

687   The traits and measures here (e.g. height, coverage, canopy area, and 3DCI) do not just relate to N

688   treatments, but they also closely connect with many aspects of genetic variation in crop performance.

689   For example, crop height is an important factor in assessing risk to crop lodging, 3D canopy area and

690   2D ground coverage are good indicators for managing agricultural inputs to optimise canopy structure

691   for radiation capture, photosynthetic output and transpirational water loss. It is also important to note

692   that such traits are only apparent in the context of a population in plots, and most of these traits are

693   difficult or impossible to convey by phenotyping individual plants in controlled environments.

694   Canopy-level traits are affected by variety, soil characteristics and agronomic factors such as seed

695   spacing and the application of plant growth regulators. The accuracy of plant models that attempt to

696   simulate the effects of these factors and their interactions on crop performance could be improved by

697   supplying them with traits presented here that were collected across a wide range of scenarios.

698   The 3D traits derived from LiDAR data such as 3DCI have many underlying component traits and

699   spatial features. A better understanding of the bases of 3DCI would broaden its application for other

700   crop improvement programmes. For instance, height variances within a plot could be due to a variety

701   of reasons: 1) a mixed population of plants with different genes controlling height, or that major

702   height genes are not fixed, but still segregating in the population; 2) agronomic or environmental

703   variability within the plot that is not related to genotypes; and 3) as 3DCI is affected by height as well

704   as spike density, it is likely that the analysis of 3D point clouds could pick up the differences in height

705   of the mainstem, different tillers on each plant, and tillering responds both to N treatment and

706   genotype (Power and Alessi, 1978).

707   Another biological application of the CropQuant-3D system is for discovery of robust quantitative

708   trait loci (QTL) for agronomic traits, which requires phenotypic data on large mapping populations

709   across multiple field environments (Griffiths et al., 2012). The high-throughput capabilities of this

710   combined system are well suited to this scale of research. A similar research approach has been

711   reported in our recent work, SeedGerm (Colmer et al., 2020), which was applied to detect genetic

712   differences in *Brassica napus* based on a range of seed germination traits. Although more work is

713   needed, greater automation of phenotypic analysis and improvements in accuracy are likely to

714   accelerate genetic analysis of crop performance under varied treatments or environments.

715   Beyond existing 3D trait analysis, continuous phenotypic analysis in 3D of different crop species is

716   likely to extend our understandings of the physiological bases of crop growth and development, for

717   which the open-source nature of CropQuant-3D is likely to be valuable for the research community.

718   There is an additional analytic power in examining longitudinal traits (time-series measures of traits

719   that change as the crop develops and matures), which can describe the dynamic interactions between

720   crop genotypes and N responses. By streamlining both the data acquisition and data analysis of field

721   phenotyping with the backpack LiDAR and CropQuant-3D, it becomes possible to obtain measures at

722   each key growth stage and at different test locations and environments, which was difficult to achieve

723   with systems that are less portable and flexible in operation, with limited opportunity to expand or

724   alter the use of the analysis software. With the approach introduced here, multi-environment 3D traits

725   collected along a time series on large genotype collections could enable a deeper understanding of the

726   genetic and physiological bases of efficient use of N for crop growth and development, as well as how

727   these responses are modulated by the environment. Technically, other than some supervised machine

728   learning algorithms, we have not embedded popular deep learning techniques into the analysis

729   pipeline for 3D traits analysis. Continuous development will improve our work, opening 3D

730   phenotypic analysis to non-expert users and computational biologists who are willing to extend and

731   jointly develop the platform. Overall, we believe that the combined backpack LiDAR and CropQuant-

732   3D system could have a great potential to advance large-scale and multi-location field phenotyping,

733   3D phenotypic analysis, and genetic studies for both crop research and breeding applications.

734

735   *Issues associated with the backpack LiDAR and CropQuant-3D*

736   Despite clear advantages, it is important to point out limitations of the combined solution. LiDAR

737   technology has been maturing very rapidly in recent years. The Robin backpack LiDAR used in this

738 study is already being replaced by newer models with better accuracy, effective scan range, and a

739 lower purchase price (the price of LiDAR devices has decreased over 30% since 2018;

740 www.yole.fr/LiDAR_Market_Update_Livox_LiDAR.aspx). Although this type of LiDAR is more

741 affordable than other large-scale systems, it is worth noting that, depending on the laser scanner

742 integrated in a backpack LiDAR device, the equipment is still relatively expensive. We compared the

743 costs of Robin with some representative backpack LiDAR systems, as well as other LiDAR-based

744 mapping approaches (**Supplemental Table S7**; information regarding GPS and RTK accuracy can be

745 found via the links in the References column). However, it is also notable that the integration and

746 mobility features of backpack LiDAR possess a unique opportunity for the community to explore

747 shared services or community-driven facilitates encouraged by EMPHASIS and AnaEE (Roy et al.,

748 2017).

749 Additionally, our software was not designed to address many colour- or spectral-related traits that

750 are also important for crop performance. For example, senescence of the lower canopy due to

751 differential N or water limitation. Adjustments to how the LiDAR is used and the associated analysis

752 algorithms would be required to capture such traits in future work. However, similar issues can be

753 applied to most of the LiDAR systems. Moreover, it was difficult to scan the lower part of the crop

754 after the canopy closure, which could cause errors to estimate above-ground biomass with stems

755 included. Also, due to field conditions such as wind movement of the plants, it is extremely

756 challenging to generate a very high-resolution and high-precision 3D model to analyse an individual

757 plant within the plot, even with high-end laser scanners or close-up 3D mapping modes. Alternative

758 3D points registration algorithms are therefore needed to deal with plant movement and reliable plant-

759 level 3D modelling.

760 The CropQuant-3D system is capable of automating the segmentation of hundreds of plots for trait

761 analysis, but the algorithm is likely to fail at the seedling development and tillering stages (GS10~29).

762 This is because the early crop height map and the gaps between drilled plants are too big to ensure a

763 meaningful plot segmentation. However, as stems elongate and crop height increases (e.g. from the

764 jointing stage onwards, GS31), our system can perform reliable plot-level masking. Another technical

765 issue that needs to be taken into consideration is the request for a user to select plot(s) to extract plot-

766   level point clouds. Although plot-level point clouds are not required for the trait analysis reported here,

767   a user is required to select one or multiple plots on the 2D CHM to extract associated point clouds,

768   which can be laborious if point clouds from hundreds of plots need to be extracted. For this technical

769   constraint, automated plot-level 3D points extraction is required and recent reports suggest they are

770   within reach (Walter et al., 2019; Roussel et al., 2020; Jin et al., 2021).

771   Lastly, because we have applied the 3D-to-2D analysis approach, some spatial information might be

772   lost during the 3D-to-2D transformation, which could reduce the accuracy when the research interest

773   is beneath the canopy region. For this loss of accuracy during the transformation, we have performed

774   some testing using 3D point cloud files collected by other equipment such as drone and vehicle

775   mounted LiDAR (**Figs. 3d&e**) to carry out multi-scale point cloud processing. Although the

776   preliminary is promising, further development and testing are still required to make the platform more

777   compatible with these types of point cloud data. Next steps of the research also need to expand the

778   application of CropQuant-3D to the analysis of different crop species so that the algorithms developed

779   for wheat can be used for addressing similar biological problems in other crop species.

780

781   *Conclusion*

782   The requirement of obtaining accurate and meaningful measures of the field phenotype at sufficient

783   scale, throughput, cost and multiple locations create a bottleneck in today's crop research and

784   breeding, which is preventing us from making full use of genomic resources for crop improvement

785   programmes. Backpack LiDAR has obvious advantages for large-scale field experiments and

786   breeding trials. The device is easy to transport and use, overcoming the main limitations of fixed

787   phenotyping platforms and can be used for multi-site data collection and at multiple time points.

788   However, the ability to process and analyse large datasets with minimal time and standard computing

789   power has limited the wide application of LiDAR-based phenotyping. To address this, we have

790   developed CropQuant-3D, which processes large LiDAR-derived 3D point cloud data and consists of

791   original algorithms packaged into a user-friendly GUI software to output multiple 3D canopy traits

792   (e.g. 3DCI) at the plot level. In a case study of 11 wheat varieties grown under three levels of N inputs,

793   analysis results obtained by by combining a backpack LiDAR and the CropQuant-3D software

794 showed that wheat varieties could be classified into different N response groups according to a range

795 of 3D traits that relate to spike density (SN m^{-2}) and grain yield. This indicates that the combined

796 solution could be a useful tool to make selections for NUE, and to dissect the physiological

797 mechanisms and genetic regulation of NUE. Hence, we trust that the system presented here has a

798 great potential to relieve some of the current bottleneck in large-scale field phenotyping for crop

799 research and breeding.

800

801 **Materials and Methods**

802 *Plant material and field experiments*

803 In the first season (2018/2019), 105 Chinese winter wheat (*Triticum aestivum*) varieties were planted

804 at the Zhenjiang Agricultural Technology Innovation Center (ZATIC, 31°57'N, 119°18'E, Jiangsu

805 province, China), measured using CropQuant-3D and assessed for yield and N responses. A subset of

806 54 varieties (**Supplemental Materials S9**) were chosen out of the 105 lines for the 2019/2020 season.

807 The selected 54 Chinese winter wheat varieties used in the field experiments were cultivated from the

808 wheat plantation regions of the middle and lower reaches of the Yangtze river, which were shown

809 previously to vary in performance and yield under different nitrogen (N) treatments (Feng et al., 2008).

810 A split-plot design was used, with three levels of N fertilisation as main plots, containing three

811 replicates of the 54 varieties as sub-plots (162 plots per N experiment). The overall size of the

812 2019/20 field trial was 486 plots, covering approximately 0.5 ha (**Fig. 1a**). For the purposes of

813 explaining the methods, data from 11 of the 54 varieties are shown.

814

815 *Crop management*

816 Before sowing, soil samples (for 0-25 cm soil layer) were measured to ensure that available N content

817 was suitable for N response studies (**Table 2**). Following standard crop management guidelines

818 (Godwin et al., 2003) and local practice, base fertiliser (P$_2$O$_5$ and K$_2$O) was applied before drilling.

819 Three levels of N fertiliser treatments were applied by hand (0, 180, and 270 kg N ha^{-1}) in two splits:

820 50% at sowing and 50% at jointing (GS31). Crops were planted in 6 m^2 plots (2×3 m), with 6 rows

821 per plot at 15 cm spacing, with 30 cm gaps between plots (**Fig. 1a**; trial plans in **Supplemental Table**

30

822   **S8**). The planting density was 2.4 million plants per hectare. Plant growth regulator was not applied in

823   the season so that stem elongation could respond unimpeded to different levels of N treatments.

824

825   *Manual measurement*

826   To collect reliable ground truth data for validating and improving CropQuant-3D's analysis algorithm,

827   a team of five field workers performed the manual scoring. They conducted a range of manual

828   measures at key growth stages (from heading, GS51-59, to grain filling, GS71-89), including plant

829   height, growth stage scoring, and key yield components such as spike number density (SN m^{-2}), spikes

830   per plant, grain number per unit area (GN m^{-2}), and thousand grain weight (TGW). For example,

831   manual plant height measures of five typical plants per plot were conducted on 11th, 18th and 26th May

832   2020, from which the scores on 18th May (two days after the LiDAR mapping, 16th May 2020) were

833   used for correlation studies in this work. As there were variances in height across the plot, three one

834   metre-square regions were selected to represent height variances within a plot. Then, all plants in the

835   region were measured and the average height value was recorded as the plot height value. When

836   measuring the plant height, the distance from the ground to the top of the ear was measured with a

837   steel ruler. We took steps to standardise manual measurements: (1) cross-scoring same traits with

838   different field workers, (2) cross-validating scores across experiments using historic data, and (3)

839   using trimmed mean to remove outlier values before calculating the average of ground truth. At

840   maturity, yield was measured in a 1 m^2 quadrat centred in the plot, from which ears were removed

841   with a sickle. Threshing was carried out with a plot thresher; any grain that passed through the

842   thresher were manually recovered from the sieved straw.

843

844   *The backpack LiDAR system*

845   The backpack LiDAR (Robin Precision, 3DLasermapping; purchased by GeoSLAM, Nottingham, UK)

846   integrates a laser scanner (RIEGL VUX-1) and three mapping settings, employing accurate GPS-

847   tagged navigation, and was used in conjunction with a real-time kinematic (RTK) base station for

848   precise positioning. The system is a lightweight (around 10 kg) and comprises high-performance laser

849   mapping system (360° scanning angle with an effective scan range of 3-200 m; further detail

850   in **Supplemental Methods S5**). Measurements focussed on the key growth stages (Zadocks et al.,

851   1974), from heading (GS51-59) to grain filling (GS71-89) when canopy structural features were

852   largely established. Standard pre-processing software packages were bundled with the device. To

853   capture the peak height for the selected wheat varieties, the trial was mapped from April to May 2020.

854   In our preliminary work, similar 3D field mapping was conducted in paddy rice trials at the Tuqiao

855   crop breeding and cultivation centre (Jiangsu China) and at the Chinese Academy of Sciences' (CAS)

856   Songjiang crop research center (Shanghai China, **Supplemental Figures S5&S6**). CropQuant-3D is

857   not bundled with Robin and can be used to analyse point cloud files generated by other sources.

858

859   *GUI-based software development*

860   To develop the GUI-based analysis software for CropQuant-3D, we utilised PyQt5, a comprehensive

861   set of Python bindings for the Qt v5 library (pypi.org/project/PyQt5/), which was developed using

862   C++ and is cross-platform for modern desktop (e.g. Windows and Mac OS) and mobile (e.g. Android

863   and iOS) systems. The GUI software we developed follows a traditional desktop-based user interface

864   development, which can be easily modified to operate in a web browser such as Google Chrome.

865   Anaconda Python release (docs.continuum.io/anaconda/install/windows) was employed as our

866   integrated development environment, through which third-party libraries required for the software

867   implementation, testing and packaging were managed by multiple virtual environments installed into

868   the `conda` directory (Virtanen et al., 2020). Algorithms (in Jupyter notebooks), GUI software (in EXE

869   format), Python-based source code and testing files (in LAS format) are freely available.

870

871   *Software implementation*

872   To implement *Step 1* (denoising) in the analysis pipeline introduced in the **Results** section, we first

873   used the `file.File` function in the laspy library to read the input file, followed by the

874   `spatial.cKDTree` function in the Scipy library to index the 3D coordinates of all the points in the

875   LAS file. Then, we applied the filtering criteria (i.e. $avg. + k \times std.$) to index outliers in the point

876   clouds and saved the denoised point cloud data using the function `file.File` (in LAS format).

877   For the *Step 2* (filtering) in the pipeline, we developed three approaches to process point cloud files

878   generated through different approaches: (1) for the backpack LiDAR mapping, we used the function

879   `lidar_ground_point_filter` in the WhiteboxTools library to filter the point cloud; (2) for UAV-

880   SfM generated pint cloud files, we employed the function `do_filtering` in the CSF library to

881   separate ground-level 3D points from above-ground points; (3) for the gantry-mounted LiDAR files,

882   because the 3D points have already been filtered, we could use the files directly.

883   For the *Step 3* (the generation of CHM) in the pipeline, we also developed three approaches to

884   process different types of point cloud files: (1) for the backpack LiDAR generated files, we applied

885   the function `lidar_tin_gridding` in the WhiteboxTools library to output CHMs with the

886   resolution parameter set as 1 cm/pixel; (2) for UAV-SfM files, we used the `lidar_tin_gridding`

887   function to output digital earth model (DEM) and DSM, followed by the

888   `clip_raster_to_polygon` function to rectify the DSM and DEM's resolution using the shapefile

889   (the .shp file collected by RTK), resulting in an CHM imaging produced through subtracting the DEM

890   from the DSM; (3) for the gantry LiDAR files, the `lidar_nearest_neighbour_gridding`

891   function was used to produce the CHM image.

892   For the *Step 4* (the definition of ROI) in the pipeline, we used the function `read_csv` in the pandas

893   library to read the geo-coordinates of the point cloud files, followed by the `open` function in the

894   rasterio library to open the CHM and convert the geo-coordinates to pixel coordinates so that 3D point

895   clouds could be analysed in 2D. The function `getPerspectiveTransform` in the OpenCV library

896   was employed to obtain the perspective transformation matrix together with the `warpPerspective`

897   function in OpenCV to define the ROI in the 2D CHM. Finally, the `io.imsave` in the scikit-image

898   library was used to save the aligned 2D CHM within ROI.

899   For the *Step 5* (plot segmentation) in the pipeline, the optional input parameters such as the number

900   of rows and columns could be used to generate horizontal and vertical base lines to assist the plot

901   segmentation. Using the `threshold_sauvola` and `threshold_local` functions in scikit-image,

902   we could obtain the threshold mask of the CHM image. Then, we applied the `sobel` function in

903   scikit-image to detect edges in the CHM, followed by the `hough_line` function to fit vertical and

904 horizontal lines, separately. By merging the detected lines and base lines, we could generate the final

905 mask representing the plot boundaries in the field.

906   For plot-based 2D/3D trait analysis, we mainly used the `regionprops` function in scikit-image to

907 calculate phenotypic traits in each plot. The plot-level 3D canopy traits were based on the

908 `clip_lidar_to_polygon` function in WhiteboxTools to crop plot-level point clouds. The source

909 code produced from the above software implementation can be seen in **Supplemental Methods S2-**

910 **S4**, as well as from our GitHub repository.

911

912 *Software profiling*

913 We profiled the GUI software using a range of testing point cloud files (in LAS format, available on

914 our GitHub repository), which were acquired by the backpack LiDAR (403 MB; 15,090,552 points),

915 UAV SfM generated point clouds (596 MB; 18,372,420 points), and gantry LiDAR (FieldScan^{TM},

916 1.42 GB; 58,446,207 points). Three Windows laptop computers with different hardware

917 configurations were used for the software profiling: (1) Intel Core i5 with 8GB memory (budget

918 laptop); (2) Intel Core i7 processor and 24GB memory (middle-end laptop); and (3) Intel Core i9 with

919 32 GB memory (high-end laptop). As the CropQuant-3D software did not support GPU acceleration,

920 both CPU and memory influenced the processing performance of CropQuant-3D. By averaging the

921 computational time (using the `time` module in Python) used by the three computers, we provided

922 details on the processing time using the three types of testing files at each step (**Supplemental Table**

923 **S10**).

924

925 **Availability and requirements**

926 Project name: 3D field phenotyping for wheat using backpack LiDAR and CropQuant-3D

927 Project home page: https://github.com/The-Zhou-Lab/LiDAR

928 Source code: https://github.com/The-Zhou-Lab/LiDAR/releases/tag/V2.0

929 GUI software: https://github.com/The-Zhou-Lab/LiDAR/releases/tag/V2.0

930 Programming language: Python 3.7

931   Requirements: Laspy (1.7.0), Whitebox (1.3.0), GDAL (3.1.4), Rasterio (1.1.8), Open3D (0.11.2),

932   Mayavi (4.7.2), Scikit-Image (0.17.2), OpenCV-Python (4.4.0.46), Pandas (1.1.5), Numpy(1.19.4),

933   Matplotlib(3.3.3), and Scipy (1.5.3).

934   License: The MIT License for open-source initiative (https://opensource.org/licenses/MIT)

935

936   **Abbreviations**

937   Comma-separated values (CSV), nitrogen use efficiency (NUE), internet of things (IoT), unmanned

938   aerial vehicle (UAV), Light Detection and Ranging (LiDAR), three-dimensional (3D), computed

939   tomography (CT), red-green-blue (RGB), global navigation satellite system (GNSS), canopy height

940   model (CHM), Zhenmai (ZM), Ningmai (NM), operating system (OS), nitrogen (N), spikes number

941   per unit area (SN m^{-2}), grain number per unit area (GN m^{-2}), thousand grain weight (TGW), real-time

942   kinematic (RTK), global positioning system (GPS), regions of interest (ROI), k-nearest neighbours

943   (kNN), graphical user interface (GUI), root-mean-square error (RMSE), discrete Fourier transform

944   (DFT), Structure from Motion (SfM), 3D voxel index (3DVI), 3D profile index (3DPI), 3D canopy

945   index (3DCI), research and development (R&D).

946

947   **Availability of supporting data**

948   The datasets supporting the results presented here are available at https://github.com/The-Zhou-

949   Lab/LiDAR/releases/tag/V2.0. Source code and other supporting data are openly available on request.

950

951   **Supplemental Data**

952   **Supplemental Figure S1.** Canopy structural curves of four wheat varieties (n = 31 plots), ZM-4,

953   NMzi-1019, ZM-5 and ZM-11, which were classified into Class One due to their similar nitrogen-

954   response patterns.

955

956 **Supplemental Figure S2.** Canopy structural curves of three wheat varieties (n = 23 plots), NMzi-1,

957 ZM-10 and ZM-12, which were classified into Class Two due to similar nitrogen-response patterns.

958

959 **Supplemental Figure S3.** Canopy structural curves of two wheat varieties (n = 15 plots), NM-26 and

960 ZM-8, which were classified into Class Three due to similar nitrogen-response patterns.

961

962 **Supplemental Figure S4.** Canopy structural curves of two wheat varieties (n = 12 plots), ZM-168

963 and ZM-09196, which were classified into Class Four due to similar nitrogen-response patterns.

964

965 **Supplemental Figure S5**. The backpack LiDAR used in three experimental fields at Tuqiao field

966 center (Jiangsu China), examining 1,458 1 m^2 rice plots under two levels of nitrogen treatments (i.e.

967 180 and 270 kg N ha^{-1}).

968

969 **Supplemental Figure S6.** The backpack LiDAR used in an experimental field at Songjiang crop

970 research center (Shanghai China), examining 261 1 m^2 rice landraces.

971

972 **Supplemental Table S1.** CropQuant-3D-measured crop height values for 486 six-metre plots (54

973 wheat varieties with three replicates) under three nitrogen (N) treatments (0, 180 and 270 kg N ha^{-1}).

974

975 **Supplemental Table S2.** CropQuant-3D's traits analyses of 81 six-metre plots of ZM & NM varieties

976 under three nitrogen (N) treatments (0, 180 and 270 kg N ha^{-1}), generated by the graphical user

977 interface (GUI) based software.

978

979 **Supplemental Table S3.** Plot-based correlation performance metrics evaluate CropQuant-3D-

980 measured height values using manual height measurement under three nitrogen (N) treatments (0, 180

981 and 270 kg N ha^{-1}).

982

983   **Supplemental Table S4.** Variety-based correlation performance metrics evaluate CropQuant-3D-

984   measured height values using manual height measurement under three nitrogen (N) treatments.

985

986   **Supplemental Table S5.** Correlation performance metrics evaluate CropQuant-3D-measured canopy

987   surface area trait using manual grain number per unit area (GN m^{-2}) scores under three nitrogen (N)

988   treatments.

989

990   **Supplemental Table S6.** Correlation performance metrics evaluate CropQuant-3D-measured 3D

991   canopy index (3DCI) trait using manual spike number per unit area (SN m^{-2}) scores under three

992   nitrogen (N) treatments.

993

994   **Supplemental Table S7.** Cost comparison between backpack LiDAR devices, unmanned aerial

995   vehicle (UAV) airborne LiDAR, and the handheld laser scanning system, with brief technical

996   specifications.

997

998   **Supplemental Table S8.** Three split fields used to study three replicates of 54 wheat varieties under

999   three levels of nitrogen (N) fertiliser treatments (i.e. 0, 180, and 270 kg N ha^{-1}). Crops were planted in

1000   six m^2 (2×3 m) plots, 486 plots in total.

1001

1002   **Supplemental Table S9.** Soil nutrient (0-25 cm soil layer) content measured before drilling in the

1003   2019/2020 season.

1004

1005   **Supplemental Table S10.** Processing time for three types of point cloud files, collected by backpack

1006   LiDAR, unmanned aerial vehicle (UAV) Structure from Motion (SfM) photogrammetry, and gantry-

1007   based LiDAR, at each analysis step.

1008

1009 **Supplemental Methods S1.** A step-by-step user guide of how to use the graphical user interface

1010 (GUI) based CropQuant-3D software to perform 3D trait analysis of point cloud datasets collected by

1011 backpack LiDAR, unmanned aerial vehicle (UAV) Structure from Motion (SfM) photogrammetry and

1012 gantry-based LiDAR.

1013

1014 **Supplemental Methods S2.** Python-based code fragments for pre-processing LiDAR-collected point

1015 cloud datasets.

1016

1017 **Supplemental Methods S3.** Python-based code fragments for automatically segmenting plots using

1018 the pre-processed LiDAR point cloud datasets.

1019

1020 **Supplemental Methods S4.** Python-based code fragments for performing plot-based 3D trait

1021 analysis, including the measurement of canopy structural variation such as 3D canopy index (3DCI).

1022

1023 **Supplemental Methods S5.** The introduction of the backpack LiDAR device, Robin Precision^{TM},

1024 used in this study.

1025

1026 **Supplemental Movie S1.** An instructional video showing how to use CropQuant-3D in action.

1027

1036   field experiments and data analysis. We thank researchers at the JIC and the University of Cambridge

1037   for constructive suggestions. We gratefully acknowledge the hardware support of the Zealquest

1038   Scientific Technology (Shanghai China) for the backpack LiDAR used in this research.

1039

1040   **Competing interests**

1041   The authors declare no competing financial interests.

1042

1043

1044   **Tables**

1045   Table 1. *Cost comparison between backpack LiDAR devices, UAV airborne LiDAR, and the handheld*
1046   *laser scanning system, with brief technical specifications.*

LiDAR system	System costs (academic price)	Brief technical spec.	References
Robin (backpack)	US$350,000-375,000 with TerraSoild software (2018)	VUX-1 HA scanner, 1.5-200 m eff. range, 5-10 mm accuracy (outdoor)	www.3dlasermapping.com (discontinued)
BMS3D-HD (backpack)	US$310,000-330,000 with BMS3D software (2021)	HDL-32 & VLP-16 scanners, 0.5-100 m eff. range, 20 mm accuracy (outdoor)	www.viametrisbusiness.com (France)
Pegasus (backpack)	US$330,000-360,000 with local software (2021)	Dual VLP-16 scanner, 80 m eff. range, 10-30 mm accuracy (outdoor)	www.leica-geosystems.com (Switzerland)
GeoSLAM (backpack)	US$300,000-320,000 with ORBIT software (2020)	Dual ZEB Discovery scanner, 100 m eff. range, 10-30 mm accuracy (outdoor)	geoslam.com (UK)
SLAM-based (backpack)	A low-cost solution with Forest3D software (2020)	Dual Velodyne Puck VLP-16 sensors, 100 m eff. range, 30 mm accuracy	(Su et al., 2020) velodynelidar.com (US)
Airborne LiDAR	US$125,000-150,000 with SpatialExplorer (2021)	SCOUT and RANGER series, 100 m range, 50-55 mm accuracy	www.phoenixlidar.com (US)
Handheld LiDAR	US$25,000-50,000 with GeoSLAM Hub & Draw software (2021)	ZEB-Horizon scanner, 100 m eff. range, 10-30 mm accuracy	geoslam.com (UK)

1047

1048

1049 **Table 2.** *Soil nutrient (0-25 cm soil layer) content before drilling in the 2019/2020 season*

pH	Organic matter (g/kg)	NO$_3$-N (mg/kg)	Phosphate (g/kg)	Potassium (g/kg)	Total organic N (mg/kg)	Plant available Phosphate (mg/kg)	Plant available Potassium (mg/kg)
6	24.2	1.35	0.61	13.2	10.4	3.04	160

1050
1051
1052

1053 **Table 3.** *Processing time for three types of point cloud files at each analysis step*

Analysis steps	Processing time (backpack)	Display time (backpack)	Proc. time (UAV)	Disp. time (UAV)	Proc. time (gantry)	Dis. time (gantry)
Step 1	2.5-3 minutes	35-45 seconds	1.5-2 mins	25-30 seconds	N/A	N/A
Step 2	1.5-2 mins	50-60 sec.	30-40 sec.	40-50 sec.	N/A	N/A
Step 3	10-15 sec.	0.2-0.5 sec.	30-40 sec.	0.5-1 sec.	10-15 sec.	0.3-0.5 sec.
Step 4	0.5-1.5 sec.	0.3-1 sec.	0.5-1 sec.	0.5-1 sec.	0.5-1.5 sec.	0.5-1 sec.
Step 5	30-40 sec.	0.5-1.5 sec.	20-25 sec.	0.5-1 sec.	5-10 sec.	0.5-1 sec.
Step 6	5-6 sec.	N/A	3-4 sec.	N/A	1-2 sec.	N/A
Step 7	5-10 sec. per plot	N/A	4-6 sec./plot	N/A	N/A	N/A

1054
1055

1056 **Figure Legends**

1057 **Figure 1: The data acquisition procedure using a backpack LiDAR device together with raw**

1058 **point cloud data generated through pre-processing a LiDAR-acquired 3D point cloud file.**

1059 (**a**) An overhead orthomosaic image of the field trial area showing 486 six-metre winter wheat

1060 varieties with three levels of nitrogen (N) fertilisation treatments (i.e. 0, 180, and 270 kg N ha^{-1}). Red

1061 arrows represent the grid-style mapping method carried out by a LiDAR operator outside the plots. (**b**)

1062 The backpack LiDAR device (ROBIN Precision) and a real-time kinematic (RTK) base station used

1063 for 3D field phenotyping. (**c**) A high-level workflow of the pre-processing software used to generate

1064 RTK-tagged point cloud data collected by the backpack LiDAR. (**d**) The raw point clouds generated

1065 for the trial area. (**e**) Initial height-based analysis with uncalibrated 3D points, which were coloured

1066 according to z values, and example plot-level images using raw 3D points, height values, and triangle

1067 mesh.

1068

1069 **Figure 2: A high-level analysis pipeline established for processing LiDAR-acquired point clouds**

1070 **and measuring yield-related traits in 3D.**

1071 (**a**) Select a pre-processed point cloud file (in LAS format). (**b**) Remove outliers (coloured red) in the

1072 point cloud, followed by filtering methods to differentiate ground-based terrain (e.g. soil level below

1073 the crop) and above-ground (crops) 3D points. (**c**) Generate a 2D canopy height model (CHM) and

1074 define the region of interest (ROI, denoted by the four red markers) using geo-coordinates collected

1075 by the ground-based real-time kinematic (RTK) station. (**d & e**) Detect horizontal and vertical edges

1076 using the Sobel operator, followed by the application of 2D Hough transform to produce a binary

1077 mask to segment plots in the field experiments. (**f**) Measure and export 3D trait analysis results for

1078 each plot, including measured traits (CSV), processed images (JPG), and processed point cloud (LAS).

1079

1080 **Figure 3: The graphical user interface (GUI) for CropQuant-3D designed for processing 3D**

1081 **point cloud files using 2D/3D image analysis algorithms and mathematic transformation for**

1082 **analysing canopy structural traits in 3D.**

1083 (**a**) The initial GUI window of CropQuant-3D. (**b**) The GUI window after accomplishing all required

1084 analysis steps, with the progress bar showing 100%. (**c**) The intermediate results that can be displayed

1085 for each processing step integrated in the analysis procedure for processing point cloud files generated

1086 by the backpack LiDAR, including optional input parameters such as the number of rows and

1087 columns of the experimental field that users could enter to assist the algorithm for segmenting plots.

1088 (**d**) The intermediate results that can be displayed for processing point cloud files collected by

1089 unmanned aerial vehicle (UAV) aerial imaging. (**e**) The intermediate results that can be displayed for

1090 processing point cloud files generated by a gantry-mounted LiDAR system, FieldScan^{TM}.

1091

1092 **Figure 4: The pseudo-coloured uncalibrated height maps, 3D visualisation, and pseudo-coloured**

1093 **calibrated height maps of nitrogen use efficiency (NUE) wheat experiments under three**

1094 **different levels of nitrogen (N) treatments.**

1095 (**a**) The 2D Canopy Height Model (CHM) image (to the left) and 3D digital surface model (DSM)

1096 image, created using the real-time kinematic (RTK) tagged altitude height values, and the calibrated

1097 height maps (to the right), showing the average height value of the highest 10% 3D points (H_{10}) for

1098 the low-N treatment; (**b & c**) the 2D CHM, 3D DSM (left) and the calibrated height (right) images for

1099 the medium-N and high-N treatments. The unified height scale bar for the three sub-figures is shown.

1100

1101 **Figure 5: The analysis process of measuring 3D canopy surface area and canopy coverage at the**

1102 **plot level using voxels and triangular mesh for wheat varieties.**

1103 (**a**) 3D points for the canopy region using the highest 50% points (H_{50}) in a given plot. (**b**) H_{50} points

1104 projected onto the ground plane, generating pixels representing crop canopy regions, which were

1105 processed by an adaptive approach to calculate the normalised canopy coverage trait (0-1, where 1

1106 stands for 100%). (**c**) A brief analysis process of computing the 3D surface area trait using triangle

1107   mesh. (**d**) The normalised 3D surface results (0-1, where 1 stands for maximum 3D surface area in a

1108   given plot) of a wheat variety under three nitrogen treatments.

1109

1110   **Figure 6: The analysis procedure of measuring 3D canopy structure at the plot level using 2D**

1111   **CHM images and a 2D discrete Fourier transform (DFT), resulting in 3D canopy structural**

1112   **curves for separating variety responses to different nitrogen (N) treatments.**

1113   (**a**) The pseudo-coloured height images and their associated grayscale height images (intensity values

1114   correspond to height values) in a plot, under three N treatments. (**b**) Frequency spectrograms

1115   generated using 2D DFT of the grayscale height images, containing all frequencies of height values

1116   and their magnitude in the plot. (**c**) Centralised magnitude of DFT produced to enable frequency and

1117   amplitude sampling through red coloured lines on the diagonal of the image; regular patterns

1118   observable in the images with medium- and high-N treatments. (**d**) Three canopy structural curves

1119   plotted to present structural differences together with cross-sections of 3D points at the canopy level,

1120   showing the wheat variety's different responses to three N treatments as well as the procedure of

1121   computing 3D canopy index (3DCI; 0-1, where 1 stands for maximum accumulated spatial variation

1122   in a given plot) based on the curves and areas beneath the curves.

1123

1124   **Figure 7: The square of the correlation coefficient (R^2) calculated to evaluate correlations**

1125   **between height estimates, canopy surface area and 3D canopy index (3DCI) computed by**

1126   **CropQuant-3D and manual measurements in the 2019/20 field trial, at three different levels of**

1127   **nitrogen (N) fertilisation; *p*-values computed through the linear regression analysis also**

1128   **reported.**

1129   (**a**) Plot-based correlation analysis of the peak height measured by CropQuant-3D and manual height

1130   measurements. (**b**) Variety-based correlation analysis of the peak height measured by CropQuant-3D

1131   and manual height measurements. (**c**) Correlation analysis of the 3D surface area index and the grain

1132   number per unit area (GN m^{-2}) data. (**d**) Correlation analysis between 3DCI and spike numbers per

1133   square metre (SN m^{-2}). Plot means (a) and genotype means (b) are shown.

1134

1135 **Figure 8: A case study of classifying wheat varieties' nitrogen responses using the 3D canopy**

1136 **index (3DCI) and spike number per unit area for 11 varieties from the Zhenmai and Ningmai**

1137 **collections under three nitrogen (N) application levels. Error bars used in the spike number per**

1138 **metre square (SN m^{-2}) scores represent one standard error.**

1139 (**a**) The first N response class, showing canopy structural curves of ZM-4 and the associated spike

1140 number per metre square (SN m^{-2}) scores under the three nitrogen (N) treatments. Also in this class

1141 were varieties NMzi-1019, ZM-5 and ZM-1 (see **Fig. 6** for the explanation of the measure). (**b**) The

1142 second N response class, showing canopy structural curves of NMzi-1 and the associated SN m^{-2}

1143 scores under the three N treatments. Also in this class were NMzi-1, ZM-10 and ZM-12. (**c**) The third

1144 N response class, showing canopy structural curves of NM-26 and the associated SN m^{-2} scores under

1145 the three N treatments. Also in this class was ZM-8. (**d**) The fourth N response class, showing canopy

1146 structural curves of ZM-168 and the associated SN m^{-2} scores under the three N treatments. Also in

1147 this class was line ZM-09196. Values shown in corresponding colour next to each curve in the plots

1148 are computed 3DCI values.

1149

1150 **Figure 9: A performance matrix to evaluate nitrogen use efficiency (NUE) of wheat varieties**

1151 **using traits and measures for 11 wheat varieties from the Zhenmai and Ningmai collections**

1152 **under three nitrogen (N) applications.**

1153 (**a-c**) A range of canopy measures (i.e. 3DCI and canopy surface area index), plot level height, and

1154 key yield components, i.e. spike number per metre square (SN m^{-2}) and grain number per metre

1155 square (GN m^{-2}), combined to assess winter wheat varieties under three N treatments, with 15% over

1156 the trimmed mean coloured dark orange, 7.5~15% coloured light orange, -7.5~7.5% coloured yellow,

1157 -15~-7.5% coloured light blue, and -15% below the trimmed mean coloured dark blue. Selected

1158 varieties were coloured red, indicating they were ranked higher than the other varieties by the

1159 performance matrix.

1160

1161 **References**

1162 **An N, Palmer CM, Baker RL, Markelz RJC, Ta J, Covington MF, Maloof JN, Welch SM,**

1163   **Weinig C** (2016) Plant high-throughput phenotyping using photogrammetry and imaging

1164   techniques to measure leaf length and rosette area. Comput Electron Agric **127**: 376–394

1165 **Antonarakis AS, Richards KS, Brasington J, Muller E** (2010) Determining leaf area index and

1166   leafy tree roughness using terrestrial laser scanning. Water Resour Res **46**: 1–12

1167 **Araus JL, Cairns JE** (2014) Field high-throughput phenotyping: the new crop breeding frontier.

1168   Trends Plant Sci **19**: 52–61

1169 **Arnó J, Escolà A, Vallès JM, Llorens J, Sanz R, Masip J, Palacín J, Rosell-Polo JR** (2013) Leaf

1170   area index estimation in vineyards using a ground-based LiDAR scanner. Precis Agric **14**: 290–

1171   306

1172 **Barker J, Zhang N, Sharon J, Steeves R, Wang X, Wei Y, Poland J** (2016) Development of a

1173   field-based high-throughput mobile phenotyping platform. Comput Electron Agric **122**: 74–85

1174 **Bauer A, Bostrom AG, Ball J, Applegate C, Cheng T, Laycock S, Rojas SM, Kirwan J, Zhou J**

1175   (2019) Combining computer vision and deep learning to enable ultra-scale aerial phenotyping

1176   and precision agriculture: A case study of lettuce production. Hortic Res **6**: 1–12

1177 **Bucksch A, Lindenbergh RC, Menenti M** (2009) SkelTre-fast skeletonisation for imperfect point

1178   cloud data of botanic trees. *In* R Veltkamp, ed, Eurographics Work. 3D Object Retr. pp 1–8

1179 **Burnette M, Rohde GS, Fahlgren N, Sagan V, Sidike P, Kooper R, Terstriep JA, Mockler T,**

1180   **Andrade-Sanchez P, Ward R, et al** (2018) TERRA-REF data processing infrastructure. ACM

1181   IPEARC 18. ACM, Pittsburgh, pp 1–7

1182 **Butler H, Chambers B, Hartzell P, Glennie C** (2020) PDAL: An open source library for the

1183   processing and analysis of point clouds. Comput Geosci **Dec**: 104680

1184 **Cabrera-Bosquet L, Fournier C, Brichet N, Welcker C, Suard BB, Tardieu F** (2016) High-

1185   throughput estimation of incident light, light interception and radiation-use efficiency of

1186   thousands of plants in a phenotyping platform. New Phytol **212**: 269–281

1187 **Carpenter AE, Kamentsky L, Eliceiri KW** (2012) A call for bioimaging software usability. Nat

1188   Methods **9**: 666–70

1189 **Cendrero-Mateo MP, Muller O, Albrecht H, Burkart A, Gatzke S, Janssen B, Keller B, Körber**

1190 **N, Kraska T, Matsubara S, et al** (2017) Field Phenotyping: Challenges and Opportunities. Terr.

1191 Ecosyst. Res. Infrastructures. pp 53–80

1192 **Cobb JN, DeClerck G, Greenberg A, Clark R, McCouch S** (2013) Next-generation phenotyping:

1193 Requirements and strategies for enhancing our understanding of genotype-phenotype

1194 relationships and its relevance to crop improvement. Theor Appl Genet **126**: 867–887

1195 **Colmer J, O'Neill CM, Wells R, Bostrom A, Reynolds D, Websdale D, Shiralagi G, Lu W, Lou**

1196 **Q, Le Cornu T, et al** (2020) SeedGerm: a cost-effective phenotyping platform for automated

1197 seed imaging and machine-learning based phenotypic analysis of crop seed germination. New

1198 Phytol **228**: 778–793

1199 **Cooley JW, Tukey JW** (1965) An Algorithm for the Machine Calculation of Complex Fourier Series.

1200 Math Comput **19**: 297

1201 **Crain JL, Wei Y, Barker J, Thompson SM, Alderman PD, Reynolds M, Zhang N, Poland J**

1202 (2016) Development and deployment of a portable field phenotyping platform. Crop Sci **56**:

1203 965–975

1204 **Deery D, Jimenez-Berni J, Jones H, Sirault X, Furbank R** (2014) Proximal Remote Sensing

1205 Buggies and Potential Applications for Field-Based Phenotyping. Agronomy **4**: 349–379

1206 **Deery DM, Rebetzke GJ, Jimenez-Berni JA, Condon AG, Smith DJ, Bechaz KM, Bovill WD**

1207 (2020) Ground-Based LiDAR Improves Phenotypic Repeatability of Above-Ground Biomass

1208 and Crop Growth Rate in Wheat. Plant Phenomics **2020**: 1–11

1209 **Duan T, Chapman SC, Holland E, Rebetzke GJ, Guo Y, Zheng B** (2016) Dynamic quantification

1210 of canopy structure to characterize early plant vigour in wheat genotypes. J Exp Bot **67**: 4523–

1211 4534

1212 **Duan T, Zheng B, Guo W, Ninomiya S, Guo Y, Chapman SC, A TD, A BZ, C WG, C SN, et al**

1213 (2017) Comparison of ground cover estimates from experiment plots in cotton, sorghum and

1214 sugarcane based on images and ortho-mosaics captured by UAV. Funct Plant Biol **44**: 169–183

1215 **Duda RO, Hart PE** (1972) Use of the Hough Transformation to Detect Lines and Curves in Pictures.

1216 Commun ACM **15**: 11–15

1217 **Edelsbrunner H, Kirkpatrick D, Seidel R** (1983) On the shape of a set of points in the plane. IEEE

1218   Trans Inf theory **29**: 551–559

1219 **Feng W, Yao X, Zhu Y, Tian YC, Cao WX** (2008) Monitoring leaf nitrogen status with

1220   hyperspectral reflectance in wheat. Eur J Agron **28**: 394–404

1221 **Fiorani F, Schurr U** (2013) Future scenarios for plant phenotyping. Annu Rev Plant Biol **64**: 267–91

1222 **Firdousi R, Parveen S** (2014) Local Thresholding Techniques in Image Binarization. Int J Eng

1223   Comput Sci **3**: 4062–4065

1224 **Friedli M, Kirchgessner N, Grieder C, Liebisch F, Mannale M, Walter A** (2016) Terrestrial 3D

1225   laser scanning to track the increase in canopy height of both monocot and dicot crop species

1226   under field conditions. Plant Methods **12**: 1–15

1227 **Fritsche-Neto R, Borém A** (2015) Phenomics: how next-generation phenotyping is revolutionazing

1228   plant breeding. doi: 10.1007/978-3-319-13677-6

1229 **Furbank RT, Jimenez-Berni JA, George-Jaeggli B, Potgieter AB, Deery DM** (2019) Field crop

1230   phenomics: enabling breeding for radiation use efficiency and biomass in cereal crops. New

1231   Phytol **223**: 1714–1727

1232 **Furbank RT, Tester M** (2011) Phenomics - technologies to relieve the phenotyping bottleneck.

1233   Trends Plant Sci **16**: 635–44

1234 **Girardeau-Montaut D** (2015) CloudCompare - User manual v2.6.1. Stuttgart, Germany

1235 **Godwin RJ, Wood GA, Taylor JC, Knight SM, Welsh JP** (2003) Precision farming of cereal crops:

1236   A review of a six year experiment to develop management guidelines. Biosyst Eng **84**: 375–391

1237 **Good AG, Shrawat AK, Muench DG** (2004) Can less yield more? Is reducing nutrient input into the

1238   environment compatible with maintaining crop production? Trends Plant Sci **9**: 597–605

1239 **Green CF., Dawkins TCK., Hunter B** (1985) Influence of foliar applied chlormequat on radiation

1240   attenuation by winter barley canopies. J Agric Sci **105**: 213–216

1241 **Griffiths S, Simmonds J, Leverington M, Wang Y, Fish L, Sayers L, Alibert L, Orford S,**

1242   **Wingen L, Snape J** (2012) Meta-QTL analysis of the genetic control of crop height in elite

1243   European winter wheat germplasm. Mol Breed **29**: 159–171

1244 **Griffiths S, Wingen L, Pietragalla J, Garcia G, Hasan A, Miralles D, Calderini DF,**

1245 **Ankleshwaria JB, Waite ML, Simmonds J, et al** (2015) Genetic dissection of grain size and

1246 grain number trade-offs in CIMMYT wheat germplasm. PLoS One **10**: 1–18

1247 **Guo Q, Wu F, Pang S, Zhao X, Chen L, Liu J, Xue B, Xu G, Li L, Jing H, et al** (2018) Crop 3D—

1248 a LiDAR based platform for 3D high-throughput crop phenotyping. Sci China Life Sci **61**: 328–

1249 339

1250 **Haralick R, Shanmugan K, Dinstein I** (1973) Textural features for image classification. IEEE Trans

1251 Syst Man Cybern **3**: 610–621

1252 **Harkel J ten, Bartholomeus H, Kooistra L** (2020) Biomass and Crop Height Estimation of

1253 Different Crops Using UAV-Based Lidar. Remote Sens **12**: 1–18

1254 **Hirafuji M, Yoichi H** (2011) Creating high-performance/low-cost ambient sensor cloud system using

1255 OpenFS (Open Field Server) for high-throughput phenotyping. … 2011 Proc. pp 2090–2092

1256 **Holman FH, Riche AB, Castle M, Wooster MJ, Hawkesford MJ** (2019) Radiometric Calibration

1257 of 'Commercial off the Shelf' Cameras for UAV-Based High-Resolution Temporal Crop

1258 Phenotyping of Reflectance and NDVI. Remote Sens **11**: 1657

1259 **Holman FH, Riche AB, Michalski A, Castle M, Wooster MJ, Hawkesford MJ** (2016) High

1260 throughput field phenotyping of wheat plant height and growth rate in field plot trials using

1261 UAV based remote sensing. Remote Sens **8**: 1–24

1262 **Hosoi F, Omasa K** (2009) Estimating vertical plant area density profile and growth parameters of a

1263 wheat canopy at different growth stages using three-dimensional portable lidar imaging. ISPRS J

1264 Photogramm Remote Sens **64**: 151–158

1265 **Howse J** (2013) OpenCV Computer Vision with Python, 1st ed. Packt Publishing Ltd., Birmingham,

1266 UK

1267 **Hyyppä E, Yu X, Kaartinen H, Hakala T, Kukko A, Vastaranta M, Hyyppä J** (2020)

1268 Comparison of backpack, handheld, under-canopy UAV, and above-canopy UAV laser scanning

1269 for field reference data collection in boreal forests. Remote Sens **12**: 1–31

1270 **Jimenez-Berni JA, Deery DM, Rozas-Larraondo P, Condon ATG, Rebetzke GJ, James RA,**

1271 **Bovill WD, Furbank RT, Sirault XRR** (2018) High throughput determination of plant height,

1272 ground cover, and above-ground biomass in wheat with LiDAR. Front Plant Sci **9**: 1–18

1273   **Jin S, Su Y, Wu F, Pang S, Gao S, Hu T, Liu J, Guo Q** (2019) Stem-Leaf Segmentation and

1274   Phenotypic Trait Extraction of Individual Maize Using Terrestrial LiDAR Data. IEEE Trans

1275   Geosci Remote Sens **57**: 1336–1346

1276   **Jin S, Sun X, Wu F, Su Y, Li Y, Song S, Xu K, Ma Q, Baret F, Jiang D, et al** (2021) Lidar sheds

1277   new light on plant phenomics for plant breeding and management: Recent advances and future

1278   prospects. ISPRS J Photogramm Remote Sens **171**: 202–223

1279   **Kachamba DJ, Ørka HO, Gobakken T, Eid T, Mwase W** (2016) Biomass estimation using 3D

1280   data from unmanned aerial vehicle imagery in a tropical woodland. Remote Sens **8**: 1–18

1281   **Kelly D, Vatsa A, Mayham W, Ng L, Thompson A, Kazic T** (2016) An opinion on imaging

1282   challenges in phenotyping field crops. Mach Vis Appl **27**: 681–694

1283   **Kirchgessner N, Liebisch F, Yu K, Pfeifer J, Friedli M, Hund A, Walter A** (2017) The ETH field

1284   phenotyping platform FIP: A cable-suspended multi-sensor system. Funct Plant Biol **44**: 154–

1285   168

1286   **Korzeniowska K, Łącka M** (2011) Generating dem from lidar data – comparison of available

1287   software tools. Arch Photogramm Cartogr Remote Sens **22**: 271–284

1288   **Kroon D-J** (2009) NUMERICAL OPTIMIZATION OF KERNEL BASED IMAGE DERIVATIVES

1289   Dirk-Jan Kroon University of Twente , Enschede. Area

1290   **Langer RHM, Liew FKY** (1973) Effects of varying nitrogen supply at different stages of the

1291   reproductive phase on spikelet and grain production and on grain nitrogen in wheat. Aust J Agric

1292   Res **24**: 647–656

1293   **Li M, Shao MR, Zeng D, Ju T, Kellogg EA, Topp CN** (2020a) Comprehensive 3D phenotyping

1294   reveals continuous morphological variation across genetically diverse sorghum inflorescences.

1295   New Phytol **226**: 1873–1885

1296   **Li P, Zhang X, Wang W, Zheng H, Yao X, Tian Y, Zhu Y, Cao W, Chen Q, Cheng T** (2020b)

1297   Estimating aboveground and organ biomass of plant canopies across the entire season of rice

1298   growth with terrestrial laser scanning. Int J Appl Earth Obs Geoinf **91**: 102132

1299   **Li W, Niu Z, Huang N, Wang C, Gao S, Wu C** (2015) Airborne LiDAR technique for estimating

1300   biomass components of maize: A case study in Zhangye City, Northwest China. Ecol Indic **57**:

51

486–496

Lin Y (2015) LiDAR: An important tool for next-generation phenotyping technology of high

potential for plant phenomics? Comput Electron Agric **119**: 61–73

Lindsay JB (2016) Whitebox GAT: A case study in geomorphometric analysis. Comput Geosci. doi:

10.1016/j.cageo.2016.07.003

Lobet G (2017) Image Analysis in Plant Sciences: Publish Then Perish. Trends Plant Sci **22**: 559–566

Lowe DG (2004) Distinctive Image Features from Scale-Invariant Keypoints. Int J Comput Vis **60**:

91–110

Masiero A, Fissore F, Guarnieri A, Pirotti F, Visintini D, Vettore A (2018) Performance

evaluation of two indoor mapping systems: Low-Cost UWB-aided photogrammetry and

backpack laser scanning. Appl Sci **8**: 1–19

Mezirow J (1978) Perspective transformation. Adult Educ Q **28**: 100–110

Momen M, Campbell MT, Walia H, Morota G (2019) Predicting longitudinal traits derived from

high-throughput phenomics in contrasting environments using genomic Legendre polynomials

and B-splines. G3 Genes, Genomes, Genet **9**: 3369–3380

**Naito H, Ogawa S, Valencia MO, Mohri H, Urano Y, Hosoi F, Shimizu Y, Chavez AL, Ishitani

M, Selvaraj MG, et al** (2017) Estimating rice yield related traits and quantitative trait loci

analysis under different nitrogen treatments using a simple tower-based field phenotyping

system with modified single-lens reflex cameras. ISPRS J Photogramm Remote Sens **125**: 50–

62

Nguyen GN, Kant S (2018) Improving nitrogen use efficiency in plants: Effective phenotyping in

conjunction with agronomic and genetic approaches. Funct Plant Biol **45**: 606–619

Omasa K, Hosoi F, Konishi A (2007) 3D lidar imaging for detecting and understanding plant

responses and canopy structure. J Exp Bot **58**: 881–898

Panjvani K, Dinh A V., Wahid KA (2019) LiDARPheno – A low-cost LiDAR-based 3D scanning

system for leaf morphological trait extraction. Front Plant Sci. doi: 10.3389/fpls.2019.00147

Pask A, Pietragalla J, Mullan D, Reynolds M (2012) Physiological Breeding II: A Field Guide to

Wheat Phenotyping. CIMMYT. doi: 10.1017/CBO9781107415324.004

1329   **Paulus S** (2019) Measuring crops in 3D: Using geometry for plant phenotyping. Plant Methods **15**: 1–

1330   13

1331   **Pieruschka R, Schurr U** (2019) Plant Phenotyping: Past, Present, and Future. Plant Phenomics **2019**:

1332   1–6

1333   **Power JF, Alessi J** (1978) Tiller development and yield of standard and semidwarf spring wheat

1334   varieties as affected by nitrogen fertilizer. J Agric Sci **90**: 97–108

1335   **Powlson D, Norse D, Chadwick D, Lu Y, Zhang W, Zhang F** (2014) Contribution of improved

1336   nitrogen fertilizer use to development of a low carbon economy in China. World Agric **4**: 10–18

1337   **Raun WR, Johnson GV** (1999) Improving nitrogen use efficiency for cereal production. Agron J **91**:

1338   357–363

1339   **Raybould A, Quemada H** (2010) Bt crops and food security in developing countries: Realised

1340   benefits, sustainable use and lowering barriers to adoption. Food Secur **2**: 247–259

1341   **Reynolds D, Ball J, Bauer A, Davey R, Griffiths S, Zhou J** (2019a) CropSight: A scalable and

1342   open-source information management system for distributed plant phenotyping and IoT-based

1343   crop management. Gigascience **8**: 1–11

1344   **Reynolds D, Baret F, Welcker C, Bostrom A, Ball J, Cellini F, Lorence A, Chawade A, Khafif M,**

1345   **Noshita K, et al** (2019b) What is cost-efficient phenotyping? Optimizing costs for different

1346   scenarios. Plant Sci **282**: 14–22

1347   **Reynolds M, Langridge P** (2016) Physiological breeding. Curr Opin Plant Biol **31**: 162–171

1348   **Ritter N, Ruth M** (1997) The GeoTIFF data interchange standard for raster geographic images. Int J

1349   Remote Sens **18**: 1637–1647

1350   **Roitsch T, Cabrera-Bosquet L, Fournier A, Ghamkhar K, Jiménez-Berni J, Pinto F, Ober ES**

1351   (2019) Review: New sensors and data-driven approaches—A path to next generation phenomics.

1352   Plant Sci **282**: 2–10

1353   **Roussel JR, Auty D, Coops NC, Tompalski P, Goodbody TRH, Meador AS, Bourdon JF, de**

1354   **Boissieu F, Achim A** (2020) lidR: An R package for analysis of Airborne Laser Scanning (ALS)

1355   data. Remote Sens Environ **251**: 112061

1356   **Roy J, Tardieu F, Tixier-Boichard M, Schurr U** (2017) European infrastructures for sustainable

1357   agriculture. Nat Plants **3**: 756–758

1358 **Sadras VO, Richards RA** (2014) Improvement of crop yield in dry environments: Benchmarks,

1359   levels of organisation and the role of nitrogen. J Exp Bot **65**: 1981–1995

1360 **Sadras VO, Slafer GA** (2012) Environmental modulation of yield components in cereals:

1361   Heritabilities reveal a hierarchy of phenotypic plasticities. F Crop Res **127**: 215–224

1362 **Sauvola J, Pietikäinen M** (2000) Adaptive document image binarization. Pattern Recognit **33**: 225–

1363   236

1364 **Scharr H, Dee H, French AP, Tsaftaris SA** (2016) Special issue on computer vision and image

1365   analysis in plant phenotyping. Mach Vis Appl **27**: 607–609

1366 **Shearman VJ, Scott RK, Foulkes MJ** (2005) Crop Physiology and Metabolism. Physiological

1367   Processes Associated with Wheat Yield Progress in the UK. Crop Sci **185**: 175–185

1368 **Singh TR, Roy S, Singh OI, Sinam T, Singh KM** (2012) A New Local Adaptive Thresholding

1369   Technique in Binarization. Int J Comput Sci Issues **8**: 271–277

1370 **Stovall AEL, Vorster AG, Anderson RS, Evangelista PH, Shugart HH** (2017) Non-destructive

1371   aboveground biomass estimation of coniferous trees using terrestrial LiDAR. Remote Sens

1372   Environ **200**: 31–42

1373 **Su Y, Guo Q, Jin S, Guan H, Sun X, Ma Q, Hu T, Wang R, Li Y** (2020) The Development and

1374   Evaluation of a Backpack LiDAR System for Accurate and Efficient Forest Inventory. IEEE

1375   Geosci Remote Sens Lett 1–5

1376 **Su Y, Wu F, Ao Z, Jin S, Qin F, Liu B, Pang S, Liu L, Guo Q** (2019) Evaluating maize phenotype

1377   dynamics under drought stress using terrestrial lidar. Plant Methods **15**: 1–16

1378 **Summerfield M** (2015) Rapid GUI Programming with Python and Qt: The Definitive Guide to PyQt

1379   Programming. Pearson, London, UK

1380 **Sun S, Li C, Paterson AH, Jiang Y, Xu R, Robertson JS, Snider JL, Chee PW** (2018) In-field

1381   high throughput phenotyping and cotton plant growth analysis using LiDAR. Front Plant Sci **9**:

1382   1–17

1383 **Susan S, Hanmandlu M** (2013) A non-extensive entropy feature and its application to texture

1384   classification. Neurocomputing **120**: 214–225

1385 **Swarbreck SM, Wang M, Wang Y, Kindred D, Sylvester-Bradley R, Shi W, Varinderpal-Singh,**

1386   **Bentley AR, Griffiths H** (2019) A Roadmap for Lowering Crop Nitrogen Requirement. Trends

1387   Plant Sci **24**: 892–904

1388 **Sylvester-Bradley R, Kindred DR** (2009) Analysing nitrogen responses of cereals to prioritize

1389   routes to the improvement of nitrogen use efficiency. J Exp Bot **60**: 1939–1951

1390 **Tardieu F, Cabrera-Bosquet L, Pridmore T, Bennett M** (2017) Plant Phenomics, From Sensors to

1391   Knowledge. Curr Biol **27**: R770–R783

1392 **Truong-Hong L, Laefer DF, Hinks T, Carr H** (2013) Combining an angle criterion with

1393   voxelization and the flying voxel method in reconstructing building models from LiDAR data.

1394   Comput Civ Infrastruct Eng **28**: 112–129

1395 **Ubbens J, Cieslak M, Prusinkiewicz P, Stavness I** (2018) The use of plant models in deep learning:

1396   An application to leaf counting in rosette plants. Plant Methods **14**: 1–10

1397 **UN Food & Agriculture Organization** (2009) How to Feed the World in 2050. *In* FAO, ed, Proc.

1398   High-Level Expert Forum How to Feed World 2050. UN FAO, Rome, p 733

1399 **Vadez V, Kholová J, Hummel G, Zhokhavets U, Gupta SK, Hash CT** (2015) LeasyScan: A novel

1400   concept combining 3D imaging and lysimetry for high-throughput phenotyping of traits

1401   controlling plant water budget. J Exp Bot **66**: 5581–5593

1402 **Valluru R, Reynolds MP, Davies WJ, Sukumaran S** (2017) Phenotypic and genome-wide

1403   association analysis of spike ethylene in diverse wheat genotypes under heat stress. New Phytol

1404   **214**: 271–283

1405 **Virlet N, Sabermanesh K, Sadeghi-Tehran P, Hawkesford MJ, Sabermanesh P, Sadeghitehran**

1406   **K, Hawkesford MJ, Sabermanesh K, Sadeghi-Tehran P, Hawkesford MJ** (2017) Field

1407   Scanalyzer: An automated robotic field phenotyping platform for detailed crop monitoring.

1408   Funct Plant Biol **44**: 143–153

1409 **Virtanen P, Gommers R, Oliphant TE, Haberland M, Reddy T, Cournapeau D, Burovski E,**

1410   **Peterson P, Weckesser W, Bright J, et al** (2020) SciPy 1.0: fundamental algorithms for

1411   scientific computing in Python. Nat Methods **17**: 261–272

1412 **Van Der Walt S, Colbert SC, Varoquaux G** (2011) The NumPy array: A structure for efficient

1413   numerical computation. Comput Sci Eng **13**: 22–30

1414   **van der Walt S, Schönberger JL, Nunez-Iglesias J, Boulogne F, Warner JD, Yager N, Gouillart**

1415   **E, Yu T** (2014) Scikit-image: image processing in Python. PeerJ **2**: 1–18

1416   **Walter JDC, Edwards J, McDonald G, Kuchel H** (2019) Estimating Biomass and Canopy Height

1417   With LiDAR for Field Crop Breeding. Front Plant Sci. doi: 10.3389/fpls.2019.01145

1418   **Wang C, Nie S, Xi X, Luo S, Sun X** (2017) Estimating the biomass of maize with hyperspectral and

1419   LiDAR data. Remote Sens **9**: 1–12

1420   **Ward B, Brien C, Oakey H, Pearson A, Negrão S, Schilling RK, Taylor J, Jarvis D, Timmins A,**

1421   **Roy SJ, et al** (2019) High-throughput 3D modelling to dissect the genetic control of leaf

1422   elongation in barley (Hordeum vulgare). Plant J **98**: 555–570

1423   **Wu D, Guo Z, Ye J, Feng H, Liu J, Chen G, Zheng J, Yan D, Yang X, Xiong X, et al** (2019)

1424   Combining high-throughput micro-CT-RGB phenotyping and genome-wide association study to

1425   dissect the genetic architecture of tiller growth in rice. J Exp Bot **70**: 545–561

1426   **Yang W, Feng H, Zhang X, Zhang J, Doonan JH, Batchelor WD, Xiong L, Yan J** (2020) Crop

1427   Phenomics and High-Throughput Phenotyping: Past Decades, Current Challenges, and Future

1428   Perspectives. Mol Plant **13**: 187–214

1429   **Zadocks JC, CHANG TT, KONZAK CF** (1974) A decimal code for the growth stages of cereals.

1430   Weed Res **14**: 415–421

1431   **Zhang H, Li Y, Zhu JK** (2018) Developing naturally stress-resistant crops for a sustainable

1432   agriculture. Nat Plants **4**: 989–996

1433   **Zhao C, Zhang Y, Du J, Guo X, Wen W, Gu S, Wang J, Fan J** (2019) Crop phenomics: Current

1434   status and perspectives. Front Plant Sci. doi: 10.3389/fpls.2019.00714

1435   **Zhao X, Guo Q, Su Y, Xue B** (2016) Improved progressive TIN densification filtering algorithm for

1436   airborne LiDAR data in forested areas. ISPRS J Photogramm Remote Sens **117**: 79–91

1437   **Zhou J, Applegate C, Alonso AD, Reynolds D, Orford S, Mackiewicz M, Griffiths S, Penfield S,**

1438   **Pullen N** (2017a) Leaf-GP: An open and automated software application for measuring growth

1439   phenotypes for arabidopsis and wheat. Plant Methods **13**: 1–30

1440   **Zhou J, Reynolds D, Websdale D, Le Cornu T, Gonzalez-Navarro O, Lister C, Orford S,**

1441   **Laycock S, Finlayson G, Stitt T, et al** (2017b) CropQuant: An automated and scalable field

1442   phenotyping platform for crop monitoring and trait measurements to facilitate breeding and

1443   digital agriculture. bioRxiv 161547

1444   **Zhou QY, Park J, Koltun V** (2018) Open3D: A modern library for 3D data processing. arXiv 1–8

1445

Figure 1: The data acquisition procedure using a backpack LiDAR device together with raw point cloud data generated through pre-processing a LiDAR-acquired 3D point cloud file.
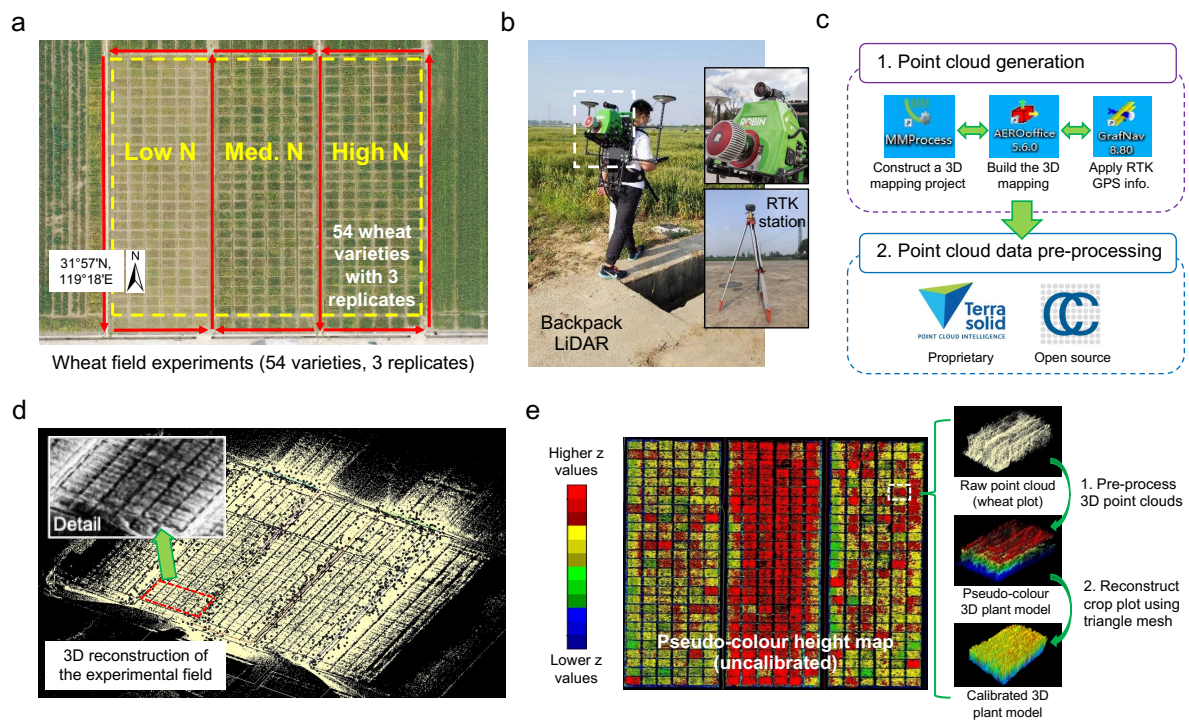
(**a**) An overhead orthomosaic image of the field trial area showing 486 six-metre winter wheat varieties with three levels of nitrogen (N) fertilisation treatments (i.e. 0, 180, and 270 kg N ha^{-1}). Red arrows represent the grid-style mapping method carried out by a LiDAR operator outside the plots. (**b**) The backpack LiDAR device (ROBIN Precision) and a real-time kinematic (RTK) base station used for 3D field phenotyping. (**c**) A high-level workflow of the pre-processing software used to generate RTK-tagged point cloud data collected by the backpack LiDAR. (**d**) The raw point clouds generated for the trial area. (**e**) Initial height-based analysis with uncalibrated 3D points, which were coloured according to z values, and example plot-level images using raw 3D points, height values, and triangle mesh.

Figure 2: A high-level analysis pipeline established for processing LiDAR-acquired point clouds and measuring yield-related traits in 3D.
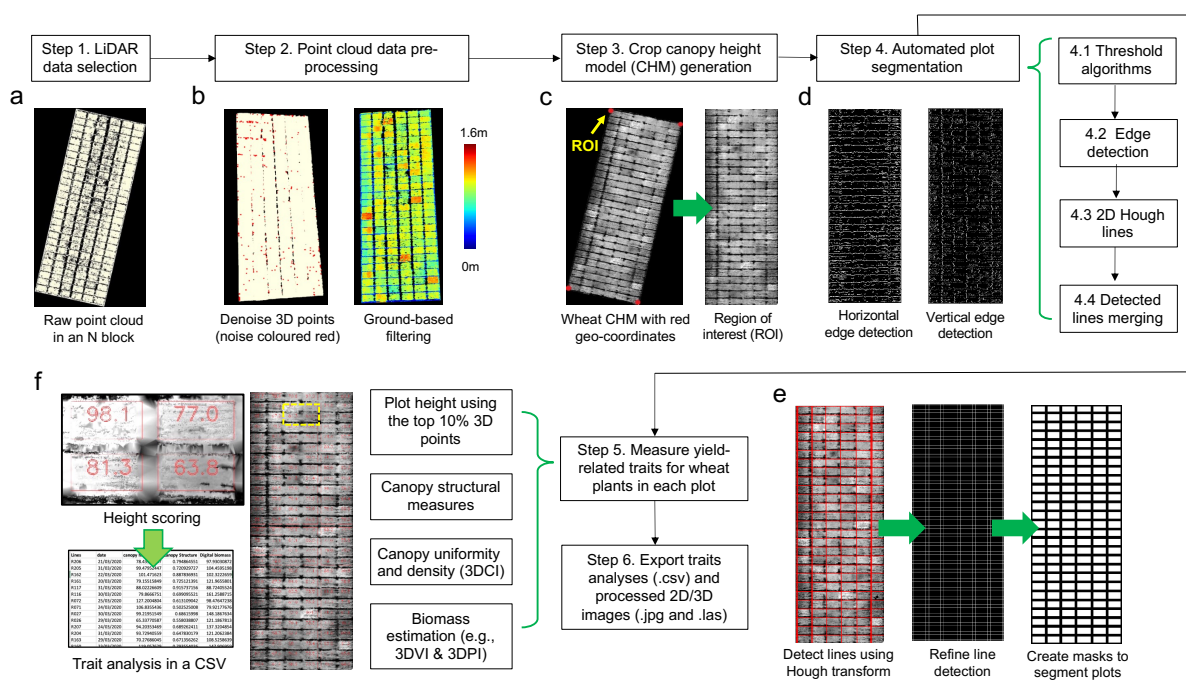
(**a**) Select a pre-processed point cloud file (in LAS format). (**b**) Remove outliers (coloured red) in the point cloud, followed by filtering methods to differentiate ground-based terrain (e.g. soil level below the crop) and above-ground (crops) 3D points. (**c**) Generate a 2D canopy height model (CHM) and define the region of interest (ROI, denoted by the four red markers) using geo-coordinates collected by the ground-based real-time kinematic (RTK) station. (**d & e**) Detect horizontal and vertical edges using the Sobel operator, followed by the application of 2D Hough transform to produce a binary mask to segment plots in the field experiments. (**f**) Measure and export 3D trait analysis results for each plot, including measured traits (CSV), processed images (JPG), and processed point cloud (LAS).

Figure 3: The graphical user interface (GUI) for CropQuant-3D designed for processing 3D point cloud files using 2D/3D image analysis algorithms and mathematic transformation for analysing canopy structural traits in 3D.
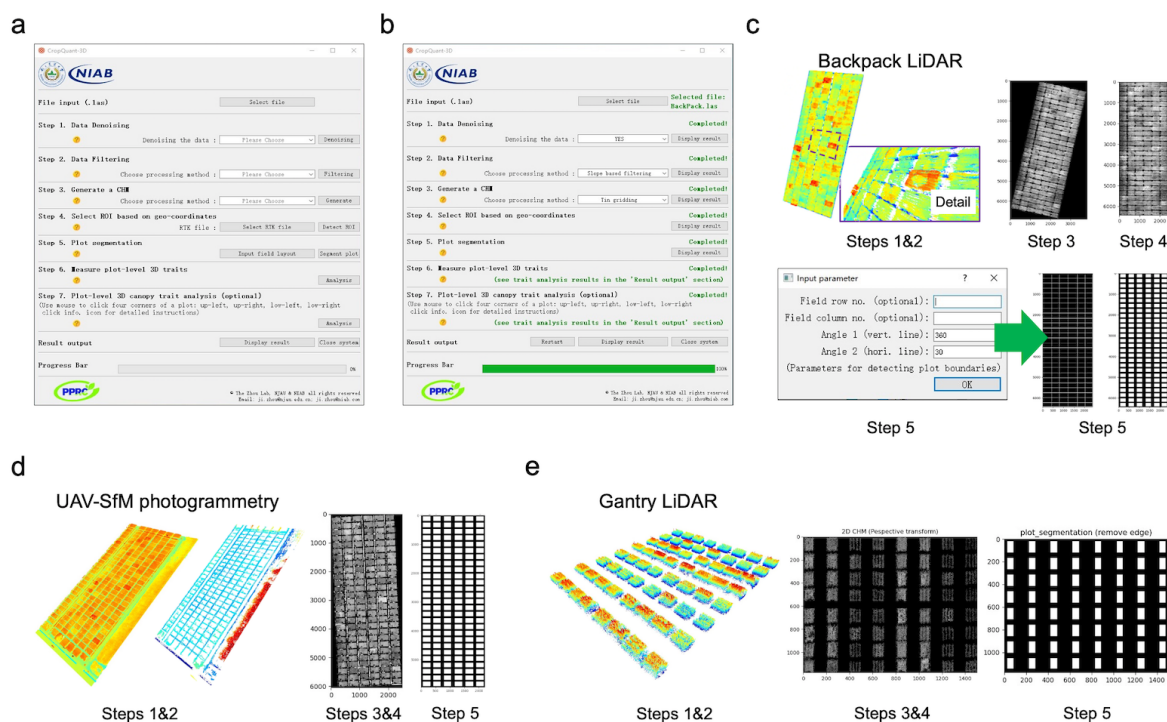
(**a**) The initial GUI window of CropQuant-3D. (**b**) The GUI window after accomplishing all required analysis steps, with the progress bar showing 100%. (**c**) The intermediate results that can be displayed for each processing step integrated in the analysis procedure for processing point cloud files generated by the backpack LiDAR, including optional input parameters such as the number of rows and columns of the experimental field that users could enter to assist the algorithm for segmenting plots. (**d**) The intermediate results that can be displayed for processing point cloud files collected by unmanned aerial vehicle (UAV) aerial imaging. (**e**) The intermediate results that can be displayed for processing point cloud files generated by a gantry-mounted LiDAR system, FieldScan[TM].

Figure 4: The pseudo-coloured uncalibrated height maps, 3D visualisation, and pseudo-coloured calibrated height maps of nitrogen use efficiency (NUE) wheat experiments under three different levels of nitrogen (N) treatments.
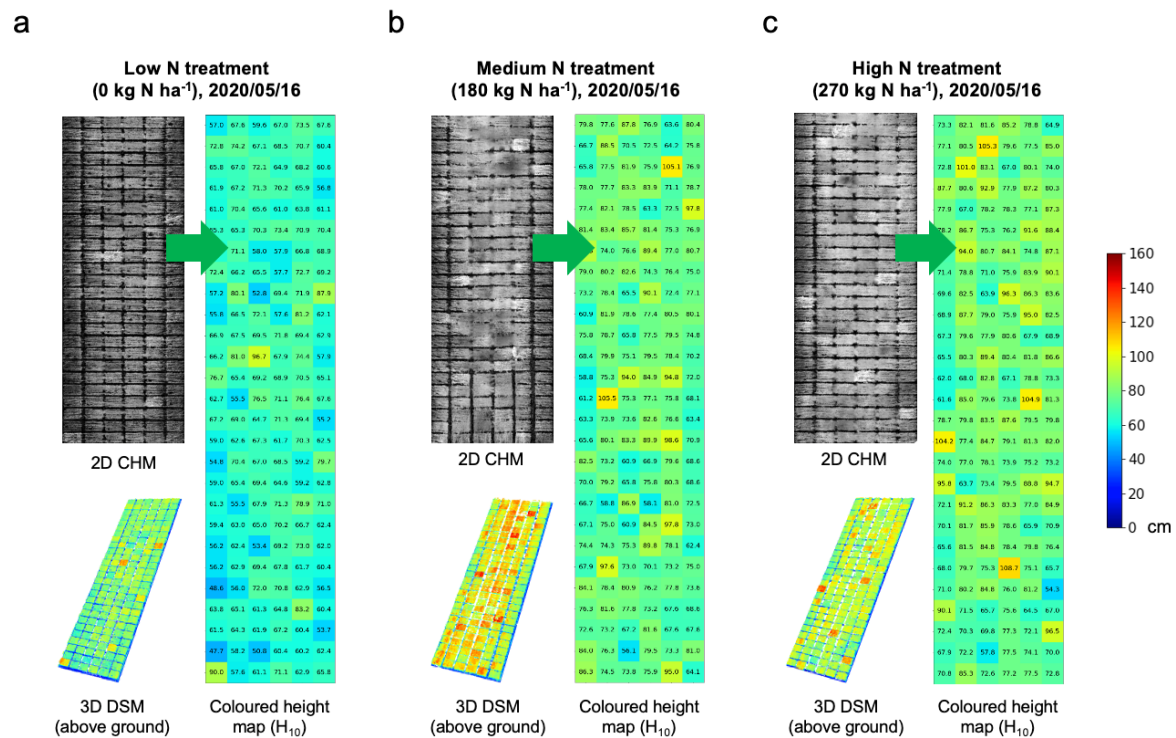
(**a**) The 2D Canopy Height Model (CHM) image (to the left) and 3D digital surface model (DSM) image, created using the real-time kinematic (RTK) tagged altitude height values, and the calibrated height maps (to the right), showing the average height value of the highest 10% 3D points (H_{10}) for the low-N treatment; (**b & c**) the 2D CHM, 3D DSM (left) and the calibrated height (right) images for the medium-N and high-N treatments. The unified height scale bar for the three sub-figures is shown.

Figure 5: The analysis process of measuring 3D canopy surface area and canopy coverage at the plot level using voxels and triangular mesh for wheat varieties.
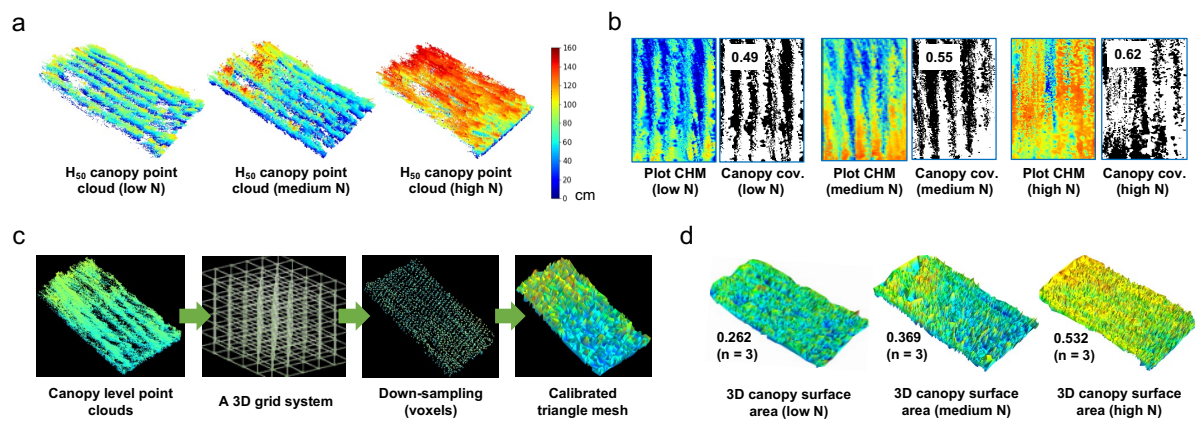
(**a**) 3D points for the canopy region using the highest 50% points (H_{50}) in a given plot. (**b**) H_{50} points projected onto the ground plane, generating pixels representing crop canopy regions, which were processed by an adaptive approach to calculate the normalised canopy coverage trait (0-1, where 1 stands for 100%). (**c**) A brief analysis process of computing the 3D surface area trait using triangle mesh. (**d**) The normalised 3D surface results (0-1, where 1 stands for maximum 3D surface area in a given plot) of a wheat variety under three nitrogen treatments.

Figure 6: The analysis procedure of measuring 3D canopy structure at the plot level using 2D CHM images and a 2D discrete Fourier transform (DFT), resulting in 3D canopy structural curves for separating variety responses to different nitrogen (N) treatments.
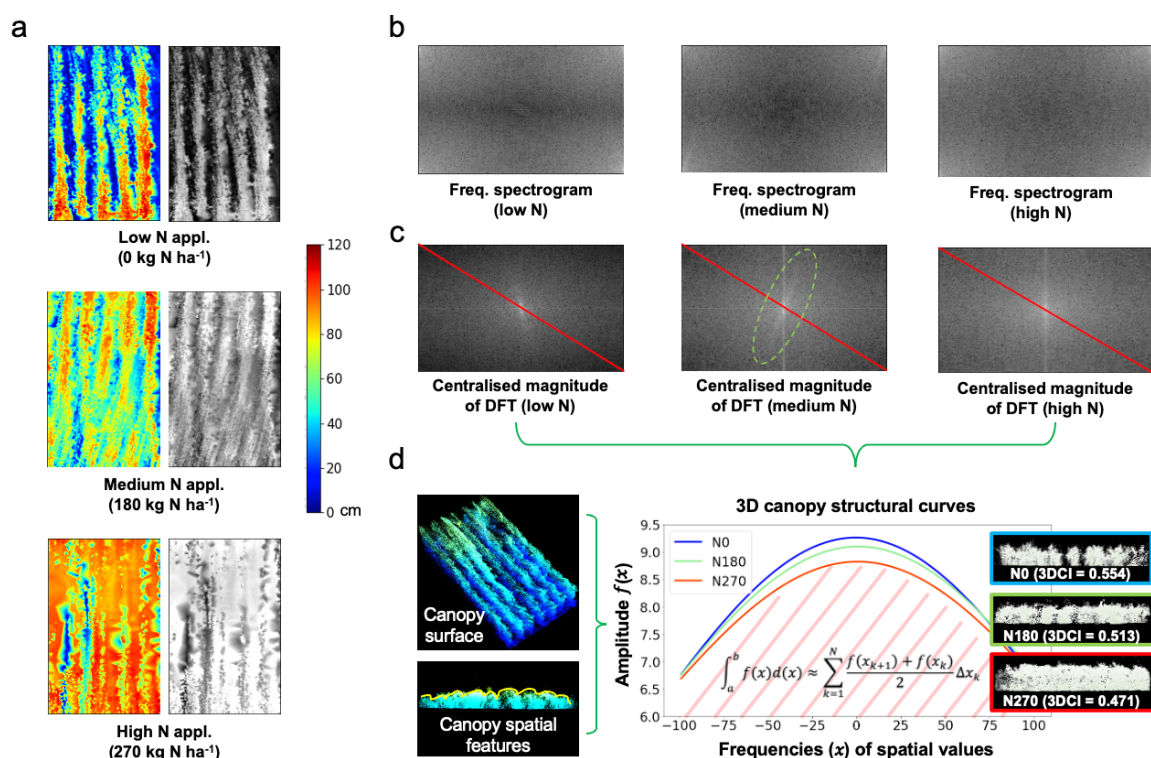
(**a**) The pseudo-coloured height images and their associated grayscale height images (intensity values correspond to height values) in a plot, under three N treatments. (**b**) Frequency spectrograms generated using 2D DFT of the grayscale height images, containing all frequencies of height values and their magnitude in the plot. (**c**) Centralised magnitude of DFT produced to enable frequency and amplitude sampling through red coloured lines on the diagonal of the image; regular patterns observable in the images with medium- and high-N treatments. (**d**) Three canopy structural curves plotted to present structural differences together with cross-sections of 3D points at the canopy level, showing the wheat variety's different responses to three N treatments as well as the procedure of computing 3D canopy index (3DCI; 0-1, where 1 stands for maximum accumulated spatial variation in a given plot) based on the curves and areas beneath the curves.

Figure 7: The square of the correlation coefficient (R^2) calculated to evaluate correlations between height estimates, canopy surface area and 3D canopy index (3DCI) computed by CropQuant-3D and manual measurements in the 2019/20 field trial, at three different levels of nitrogen (N) fertilisation; *p*-values computed through the linear regression analysis also reported.
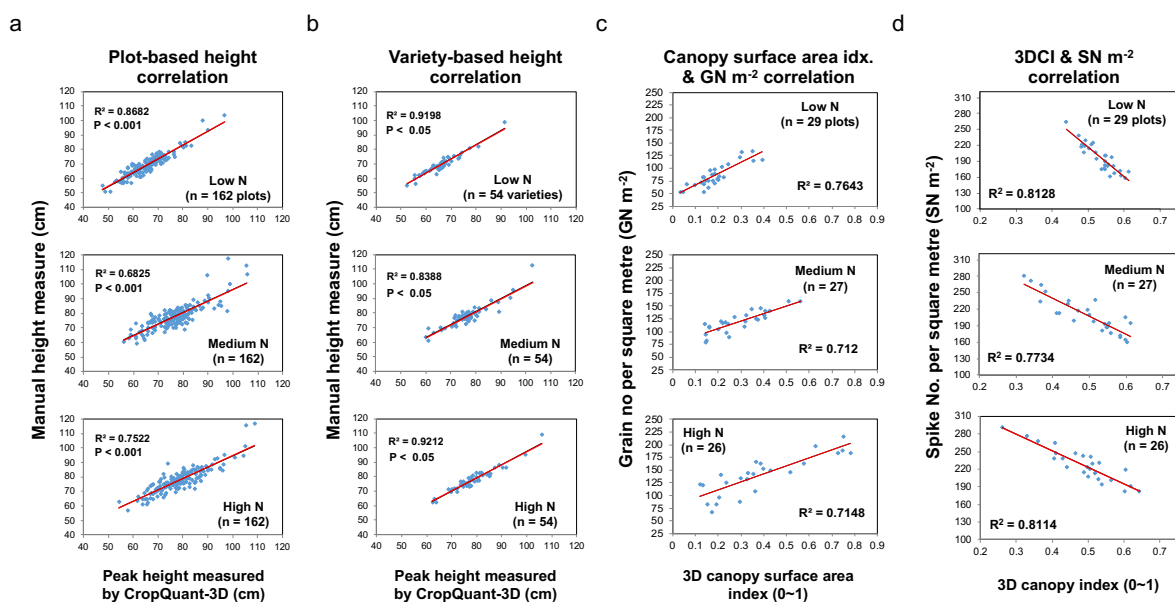
(**a**) Plot-based correlation analysis of the peak height measured by CropQuant-3D and manual height measurements. (**b**) Variety-based correlation analysis of the peak height measured by CropQuant-3D and manual height measurements. (**c**) Correlation analysis of the 3D surface area index and the grain number per unit area (GN m^{-2}) data. (**d**) Correlation analysis between 3DCI and spike numbers per square metre (SN m^{-2}). Plot means (a) and genotype means (b) are shown.

Figure 8: A case study of classifying wheat varieties' nitrogen responses using the 3D canopy index (3DCI) and spike number per unit area for 11 varieties from the Zhenmai and Ningmai collections under three nitrogen (N) application levels. Error bars used in the spike number per metre square (SN m^{-2}) scores represent one standard error.
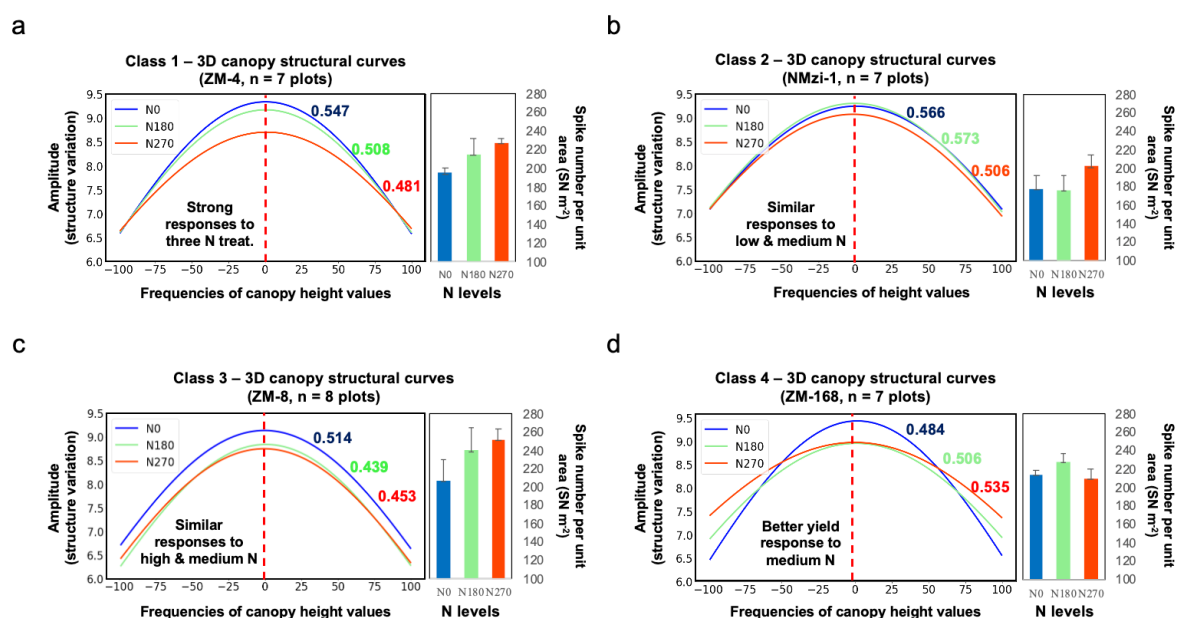
(**a**) The first N response class, showing canopy structural curves of ZM-4 and the associated spike number per metre square (SN m^{-2}) scores under the three nitrogen (N) treatments. Also in this class were varieties NMzi-1019, ZM-5 and ZM-1 (see **Fig. 6** for the explanation of the measure). (**b**) The second N response class, showing canopy structural curves of NMzi-1 and the associated SN m^{-2} scores under the three N treatments. Also in this class were NMzi-1, ZM-10 and ZM-12. (**c**) The third N response class, showing canopy structural curves of NM-26 and the associated SN m^{-2} scores under the three N treatments. Also in this class was ZM-8. (**d**) The fourth N response class, showing canopy structural curves of ZM-168 and the associated SN m^{-2} scores under the three N treatments. Also in this class was line ZM-09196. Values shown in corresponding colour next to each curve in the plots are computed 3DCI values.

Figure 9: A performance matrix to evaluate nitrogen use efficiency (NUE) of wheat varieties using traits and measures for 11 wheat varieties from the Zhenmai and Ningmai collections under three nitrogen (N) applications.

a

Low N (n = 29 plots, 11 varieties)

Lines	SN m^{-2}	GW m^{-2}	3DCI	Can_Sur	Height	Overall rank
NMzi1	2	2	3	1	3	2.3
NMzi1019	3	4	3	4	3	3.4
NM26	4	2	3	1	5	3.2
ZM4	3	5	3	3	2	3.3
ZM5	3	5	3	5	3	3.7
ZM8	4	4	3	5	3	3.7
ZM10	2	1	3	1	3	2.1
ZM11	3	2	3	3	3	2.8
ZM12	2	3	3	4	3	2.9
ZM168	5	4	4	5	2	4.0
ZM09196	4	1	4	1	5	3.2

b

Medium N (n = 27 plots, 11 varieties)

SN m^{-2}	GW m^{-2}	3DCI	Can_Sur	Height	Overall rank
1	5	1	5	3	2.8
3	2	3	2	3	2.7
4	3	5	4	4	4.0
3	3	3	3	3	3.0
3	4	4	5	2	3.5
4	3	4	1	2	3.1
2	5	1	4	3	3.0
3	2	3	2	3	2.7
1	3	1	3	3	2.1
4	3	3	5	3	3.5
5	2	5	1	4	3.7

c

High N (n = 26 plots, 11 varieties)

SN m^{-2}	GW m^{-2}	3DCI	Can_Sur	Height	Overall rank
2	4	2	5	3	3.0
3	3	3	3	3	3.0
3	5	3	5	4	3.9
2	4	2	5	2	2.8
3	3	3	2	1	2.5
4	1	4	1	2	2.6
1	3	2	3	3	2.3
3	1	5	1	3	2.7
4	3	4	3	3	3.5
3	3	1	3	2	2.4
3	3	4	2	4	3.3

(**a-c**) A range of canopy measures (i.e. 3DCI and canopy surface area index), plot level height, and key yield components, i.e. spike number per metre square (SN m^{-2}) and grain number per metre square (GN m^{-2}), combined to assess winter wheat varieties under three N treatments, with 15% over the trimmed mean coloured dark orange, 7.5~15% coloured light orange, -7.5~7.5% coloured yellow, -15~-7.5% coloured light blue, and -15% below the trimmed mean coloured dark blue. Selected varieties were coloured red, indicating they were ranked higher than the other varieties by the performance matrix.

Parsed Citations

An N, Palmer CM, Baker RL, Markelz RJC, Ta J, Covington MF, Maloof JN, Welch SM, Weinig C (2016) Plant high-throughput phenotyping using photogrammetry and imaging techniques to measure leaf length and rosette area. Comput Electron Agric 127: 376–394

Google Scholar: Author Only Title Only Author and Title

Antonarakis AS, Richards KS, Brasington J, Muller E (2010) Determining leaf area index and leafy tree roughness using terrestrial laser scanning. Water Resour Res 46: 1–12

Google Scholar: Author Only Title Only Author and Title

Araus JL, Cairns JE (2014) Field high-throughput phenotyping: the new crop breeding frontier. Trends Plant Sci 19: 52–61

Google Scholar: Author Only Title Only Author and Title

Arnó J, Escolà A, Vallès JM, Llorens J, Sanz R, Masip J, Palacín J, Rosell-Polo JR (2013) Leaf area index estimation in vineyards using a ground-based LiDAR scanner. Precis Agric 14: 290–306

Google Scholar: Author Only Title Only Author and Title

Barker J, Zhang N, Sharon J, Steeves R, Wang X, Wei Y, Poland J (2016) Development of a field-based high-throughput mobile phenotyping platform. Comput Electron Agric 122: 74–85

Google Scholar: Author Only Title Only Author and Title

Bauer A, Bostrom AG, Ball J, Applegate C, Cheng T, Laycock S, Rojas SM, Kirwan J, Zhou J (2019) Combining computer vision and deep learning to enable ultra-scale aerial phenotyping and precision agriculture: A case study of lettuce production. Hortic Res 6: 1–12

Google Scholar: Author Only Title Only Author and Title

Bucksch A, Lindenbergh RC, Menenti M (2009) SkelTre-fast skeletonisation for imperfect point cloud data of botanic trees. In R Veltkamp, ed, Eurographics Work. 3D Object Retr. pp 1–8

Google Scholar: Author Only Title Only Author and Title

Burnette M, Rohde GS, Fahlgren N, Sagan V, Sidike P, Kooper R, Terstriep JA, Mockler T, Andrade-Sanchez P, Ward R, et al (2018) TERRA-REF data processing infrastructure. ACM IPEARC 18. ACM, Pittsburgh, pp 1–7

Google Scholar: Author Only Title Only Author and Title

Butler H, Chambers B, Hartzell P, Glennie C (2020) PDAL: An open source library for the processing and analysis of point clouds. Comput Geosci Dec: 104680

Google Scholar: Author Only Title Only Author and Title

Cabrera-Bosquet L, Fournier C, Brichet N, Welcker C, Suard BB, Tardieu F (2016) High-throughput estimation of incident light, light interception and radiation-use efficiency of thousands of plants in a phenotyping platform. New Phytol 212: 269–281

Google Scholar: Author Only Title Only Author and Title

Carpenter AE, Kamentsky L, Eliceiri KW (2012) A call for bioimaging software usability. Nat Methods 9: 666–70

Google Scholar: Author Only Title Only Author and Title

Cendrero-Mateo MP, Muller O, Albrecht H, Burkart A, Gatzke S, Janssen B, Keller B, Körber N, Kraska T, Matsubara S, et al (2017) Field Phenotyping: Challenges and Opportunities. Terr. Ecosyst. Res. Infrastructures. pp 53–80

Google Scholar: Author Only Title Only Author and Title

Cobb JN, DeClerck G, Greenberg A, Clark R, McCouch S (2013) Next-generation phenotyping: Requirements and strategies for enhancing our understanding of genotype-phenotype relationships and its relevance to crop improvement. Theor Appl Genet 126: 867–887

Google Scholar: Author Only Title Only Author and Title

Colmer J, O'Neill CM, Wells R, Bostrom A, Reynolds D, Websdale D, Shiralagi G, Lu W, Lou Q, Le Cornu T, et al (2020) SeedGerm: a cost-effective phenotyping platform for automated seed imaging and machine-learning based phenotypic analysis of crop seed germination. New Phytol 228: 778–793

Google Scholar: Author Only Title Only Author and Title

Cooley JW, Tukey JW (1965) An Algorithm for the Machine Calculation of Complex Fourier Series. Math Comput 19: 297

Google Scholar: Author Only Title Only Author and Title

Crain JL, Wei Y, Barker J, Thompson SM, Alderman PD, Reynolds M, Zhang N, Poland J (2016) Development and deployment of a portable field phenotyping platform. Crop Sci 56: 965–975

Google Scholar: Author Only Title Only Author and Title

Deery D, Jimenez-Berni J, Jones H, Sirault X, Furbank R (2014) Proximal Remote Sensing Buggies and Potential Applications for Field-Based Phenotyping. Agronomy 4: 349–379

Google Scholar: Author Only Title Only Author and Title

Deery DM, Rebetzke GJ, Jimenez-Berni JA, Condon AG, Smith DJ, Bechaz KM, Bovill WD (2020) Ground-Based LiDAR Improves Phenotypic Repeatability of Above-Ground Biomass and Crop Growth Rate in Wheat. Plant Phenomics 2020: 1–11

Google Scholar: Author Only Title Only Author and Title

Duan T, Chapman SC, Holland E, Rebetzke GJ, Guo Y, Zheng B (2016) Dynamic quantification of canopy structure to characterize early plant vigour in wheat genotypes. J Exp Bot 67: 4523–4534
  Google Scholar: Author Only Title Only Author and Title

Duan T, Zheng B, Guo W, Ninomiya S, Guo Y, Chapman SC, A TD, A BZ, C WG, C SN, et al (2017) Comparison of ground cover estimates from experiment plots in cotton, sorghum and sugarcane based on images and ortho-mosaics captured by UAV. Funct Plant Biol 44: 169–183
  Google Scholar: Author Only Title Only Author and Title

Duda RO, Hart PE (1972) Use of the Hough Transformation to Detect Lines and Curves in Pictures. Commun ACM 15: 11–15
  Google Scholar: Author Only Title Only Author and Title

Edelsbrunner H, Kirkpatrick D, Seidel R (1983) On the shape of a set of points in the plane. IEEE Trans Inf theory 29: 551–559
  Google Scholar: Author Only Title Only Author and Title

Feng W, Yao X, Zhu Y, Tian YC, Cao WX (2008) Monitoring leaf nitrogen status with hyperspectral reflectance in wheat. Eur J Agron 28: 394–404
  Google Scholar: Author Only Title Only Author and Title

Fiorani F, Schurr U (2013) Future scenarios for plant phenotyping. Annu Rev Plant Biol 64: 267–91
  Google Scholar: Author Only Title Only Author and Title

Firdousi R, Parveen S (2014) Local Thresholding Techniques in Image Binarization. Int J Eng Comput Sci 3: 4062–4065
  Google Scholar: Author Only Title Only Author and Title

Friedli M, Kirchgessner N, Grieder C, Liebisch F, Mannale M, Walter A (2016) Terrestrial 3D laser scanning to track the increase in canopy height of both monocot and dicot crop species under field conditions. Plant Methods 12: 1–15
  Google Scholar: Author Only Title Only Author and Title

Fritsche-Neto R, Borém A (2015) Phenomics: how next-generation phenotyping is revolutionazing plant breeding. doi: 10.1007/978-3-319-13677-6
  Google Scholar: Author Only Title Only Author and Title

Furbank RT, Jimenez-Berni JA, George-Jaeggli B, Potgieter AB, Deery DM (2019) Field crop phenomics: enabling breeding for radiation use efficiency and biomass in cereal crops. New Phytol 223: 1714–1727
  Google Scholar: Author Only Title Only Author and Title

Furbank RT, Tester M (2011) Phenomics - technologies to relieve the phenotyping bottleneck. Trends Plant Sci 16: 635–44
  Google Scholar: Author Only Title Only Author and Title

Girardeau-Montaut D (2015) CloudCompare - User manual v2.6.1. Stuttgart, Germany
  Google Scholar: Author Only Title Only Author and Title

Godwin RJ, Wood GA, Taylor JC, Knight SM, Welsh JP (2003) Precision farming of cereal crops: A review of a six year experiment to develop management guidelines. Biosyst Eng 84: 375–391
  Google Scholar: Author Only Title Only Author and Title

Good AG, Shrawat AK, Muench DG (2004) Can less yield more? Is reducing nutrient input into the environment compatible with maintaining crop production? Trends Plant Sci 9: 597–605

Green CF., Dawkins TCK., Hunter B (1985) Influence of foliar applied chlormequat on radiation attenuation by winter barley canopies. J Agric Sci 105: 213–216
  Google Scholar: Author Only Title Only Author and Title

Griffiths S, Simmonds J, Leverington M, Wang Y, Fish L, Sayers L, Alibert L, Orford S, Wingen L, Snape J (2012) Meta-QTL analysis of the genetic control of crop height in elite European winter wheat germplasm. Mol Breed 29: 159–171
  Google Scholar: Author Only Title Only Author and Title

Griffiths S, Wingen L, Pietragalla J, Garcia G, Hasan A, Miralles D, Calderini DF, Ankleshwaria JB, Waite ML, Simmonds J, et al (2015) Genetic dissection of grain size and grain number trade-offs in CIMMYT wheat germplasm. PLoS One 10: 1–18
  Google Scholar: Author Only Title Only Author and Title

Guo Q, Wu F, Pang S, Zhao X, Chen L, Liu J, Xue B, Xu G, Li L, Jing H, et al (2018) Crop 3D-a LiDAR based platform for 3D high-throughput crop phenotyping. Sci China Life Sci 61: 328–339
  Google Scholar: Author Only Title Only Author and Title

Haralick R, Shanmugan K, Dinstein I (1973) Textural features for image classification. IEEE Trans Syst Man Cybern 3: 610–621
  Google Scholar: Author Only Title Only Author and Title

Harkel J ten, Bartholomeus H, Kooistra L (2020) Biomass and Crop Height Estimation of Different Crops Using UAV-Based Lidar. Remote Sens 12: 1–18
  Google Scholar: Author Only Title Only Author and Title

Hirafuji M, Yoichi H (2011) Creating high-performance/low-cost ambient sensor cloud system using OpenFS (Open Field Server) for high-throughput phenotyping. ... 2011 Proc. pp 2090–2092
Google Scholar: Author Only Title Only Author and Title

Holman FH, Riche AB, Castle M, Wooster MJ, Hawkesford MJ (2019) Radiometric Calibration of 'Commercial off the Shelf' Cameras for UAV-Based High-Resolution Temporal Crop Phenotyping of Reflectance and NDVI. Remote Sens 11: 1657
Google Scholar: Author Only Title Only Author and Title

Holman FH, Riche AB, Michalski A, Castle M, Wooster MJ, Hawkesford MJ (2016) High throughput field phenotyping of wheat plant height and growth rate in field plot trials using UAV based remote sensing. Remote Sens 8: 1–24
Google Scholar: Author Only Title Only Author and Title

Hosoi F, Omasa K (2009) Estimating vertical plant area density profile and growth parameters of a wheat canopy at different growth stages using three-dimensional portable lidar imaging. ISPRS J Photogramm Remote Sens 64: 151–158
Google Scholar: Author Only Title Only Author and Title

Howse J (2013) OpenCV Computer Vision with Python, 1st ed. Packt Publishing Ltd., Birmingham, UK
Google Scholar: Author Only Title Only Author and Title

Hyyppä E, Yu X, Kaartinen H, Hakala T, Kukko A, Vastaranta M, Hyyppä J (2020) Comparison of backpack, handheld, under-canopy UAV, and above-canopy UAV laser scanning for field reference data collection in boreal forests. Remote Sens 12: 1–31
Google Scholar: Author Only Title Only Author and Title

Jimenez-Berni JA, Deery DM, Rozas-Larraondo P, Condon ATG, Rebetzke GJ, James RA, Bovill WD, Furbank RT, Sirault XRR (2018) High throughput determination of plant height, ground cover, and above-ground biomass in wheat with LiDAR. Front Plant Sci 9: 1–18
Google Scholar: Author Only Title Only Author and Title

Jin S, Su Y, Wu F, Pang S, Gao S, Hu T, Liu J, Guo Q (2019) Stem-Leaf Segmentation and Phenotypic Trait Extraction of Individual Maize Using Terrestrial LiDAR Data. IEEE Trans Geosci Remote Sens 57: 1336–1346
Google Scholar: Author Only Title Only Author and Title

Jin S, Sun X, Wu F, Su Y, Li Y, Song S, Xu K, Ma Q, Baret F, Jiang D, et al (2021) Lidar sheds new light on plant phenomics for plant breeding and management: Recent advances and future prospects. ISPRS J Photogramm Remote Sens 171: 202–223
Google Scholar: Author Only Title Only Author and Title

Kachamba DJ, Ørka HO, Gobakken T, Eid T, Mwase W (2016) Biomass estimation using 3D data from unmanned aerial vehicle imagery in a tropical woodland. Remote Sens 8: 1–18
Google Scholar: Author Only Title Only Author and Title

Kelly D, Vatsa A, Mayham W, Ng L, Thompson A, Kazic T (2016) An opinion on imaging challenges in phenotyping field crops. Mach Vis Appl 27: 681–694
Google Scholar: Author Only Title Only Author and Title

Kirchgessner N, Liebisch F, Yu K, Pfeifer J, Friedli M, Hund A, Walter A (2017) The ETH field phenotyping platform FIP: A cable-suspended multi-sensor system. Funct Plant Biol 44: 154–168
Google Scholar: Author Only Title Only Author and Title

Korzeniowska K, Łącka M (2011) Generating dem from lidar data – comparison of available software tools. Arch Photogramm Cartogr Remote Sens 22: 271–284
Google Scholar: Author Only Title Only Author and Title

Kroon D-J (2009) NUMERICAL OPTIMIZATION OF KERNEL BASED IMAGE DERIVATIVES Dirk-Jan Kroon University of Twente , Enschede. Area
Google Scholar: Author Only Title Only Author and Title

Langer RHM, Liew FKY (1973) Effects of varying nitrogen supply at different stages of the reproductive phase on spikelet and grain production and on grain nitrogen in wheat. Aust J Agric Res 24: 647–656
Google Scholar: Author Only Title Only Author and Title

Li M, Shao MR, Zeng D, Ju T, Kellogg EA, Topp CN (2020a) Comprehensive 3D phenotyping reveals continuous morphological variation across genetically diverse sorghum inflorescences. New Phytol 226: 1873–1885
Google Scholar: Author Only Title Only Author and Title

Li P, Zhang X, Wang W, Zheng H, Yao X, Tian Y, Zhu Y, Cao W, Chen Q, Cheng T (2020b) Estimating aboveground and organ biomass of plant canopies across the entire season of rice growth with terrestrial laser scanning. Int J Appl Earth Obs Geoinf 91: 102132
Google Scholar: Author Only Title Only Author and Title

Li W, Niu Z, Huang N, Wang C, Gao S, Wu C (2015) Airborne LiDAR technique for estimating biomass components of maize: A case study in Zhangye City, Northwest China. Ecol Indic 57: 486–496
Google Scholar: Author Only Title Only Author and Title

Lin Y (2015) LiDAR: An important tool for next-generation phenotyping technology of high potential for plant phenomics? Comput Electron Agric 119: 61–73

Lindsay JB (2016) Whitebox GAT: A case study in geomorphometric analysis. Comput Geosci. doi: 10.1016/j.cageo.2016.07.003
Google Scholar: Author Only Title Only Author and Title

Lobet G (2017) Image Analysis in Plant Sciences: Publish Then Perish. Trends Plant Sci 22: 559–566
Google Scholar: Author Only Title Only Author and Title

Lowe DG (2004) Distinctive Image Features from Scale-Invariant Keypoints. Int J Comput Vis 60: 91–110
Google Scholar: Author Only Title Only Author and Title

Masiero A, Fissore F, Guarnieri A, Pirotti F, Visintini D, Vettore A (2018) Performance evaluation of two indoor mapping systems: Low-Cost UWB-aided photogrammetry and backpack laser scanning. Appl Sci 8: 1–19
Google Scholar: Author Only Title Only Author and Title

Mezirow J (1978) Perspective transformation. Adult Educ Q 28: 100–110
Google Scholar: Author Only Title Only Author and Title

Momen M, Campbell MT, Walia H, Morota G (2019) Predicting longitudinal traits derived from high-throughput phenomics in contrasting environments using genomic Legendre polynomials and B-splines. G3 Genes, Genomes, Genet 9: 3369–3380
Google Scholar: Author Only Title Only Author and Title

Naito H, Ogawa S, Valencia MO, Mohri H, Urano Y, Hosoi F, Shimizu Y, Chavez AL, Ishitani M, Selvaraj MG, et al (2017) Estimating rice yield related traits and quantitative trait loci analysis under different nitrogen treatments using a simple tower-based field phenotyping system with modified single-lens reflex cameras. ISPRS J Photogramm Remote Sens 125: 50–62
Google Scholar: Author Only Title Only Author and Title

Nguyen GN, Kant S (2018) Improving nitrogen use efficiency in plants: Effective phenotyping in conjunction with agronomic and genetic approaches. Funct Plant Biol 45: 606–619
Google Scholar: Author Only Title Only Author and Title

Omasa K, Hosoi F, Konishi A (2007) 3D lidar imaging for detecting and understanding plant responses and canopy structure. J Exp Bot 58: 881–898
Google Scholar: Author Only Title Only Author and Title

Panjvani K, Dinh A V., Wahid KA (2019) LiDARPheno – A low-cost LiDAR-based 3D scanning system for leaf morphological trait extraction. Front Plant Sci. doi: 10.3389/fpls.2019.00147
Google Scholar: Author Only Title Only Author and Title

Pask A, Pietragalla J, Mullan D, Reynolds M (2012) Physiological Breeding II: A Field Guide to Wheat Phenotyping. CIMMYT. doi: 10.1017/CBO9781107415324.004
Google Scholar: Author Only Title Only Author and Title

Paulus S (2019) Measuring crops in 3D: Using geometry for plant phenotyping. Plant Methods 15: 1–13
Google Scholar: Author Only Title Only Author and Title

Pieruschka R, Schurr U (2019) Plant Phenotyping: Past, Present, and Future. Plant Phenomics 2019: 1–6
Google Scholar: Author Only Title Only Author and Title

Power JF, Alessi J (1978) Tiller development and yield of standard and semidwarf spring wheat varieties as affected by nitrogen fertilizer. J Agric Sci 90: 97–108
Google Scholar: Author Only Title Only Author and Title

Powlson D, Norse D, Chadwick D, Lu Y, Zhang W, Zhang F (2014) Contribution of improved nitrogen fertilizer use to development of a low carbon economy in China. World Agric 4: 10–18
Google Scholar: Author Only Title Only Author and Title

Raun WR, Johnson GV (1999) Improving nitrogen use efficiency for cereal production. Agron J 91: 357–363
Google Scholar: Author Only Title Only Author and Title

Raybould A, Quemada H (2010) Bt crops and food security in developing countries: Realised benefits, sustainable use and lowering barriers to adoption. Food Secur 2: 247–259
Google Scholar: Author Only Title Only Author and Title

Reynolds D, Ball J, Bauer A, Davey R, Griffiths S, Zhou J (2019a) CropSight: A scalable and open-source information management system for distributed plant phenotyping and IoT-based crop management. Gigascience 8: 1–11
Google Scholar: Author Only Title Only Author and Title

Reynolds D, Baret F, Welcker C, Bostrom A, Ball J, Cellini F, Lorence A, Chawade A, Khafif M, Noshita K, et al (2019b) What is cost-efficient phenotyping? Optimizing costs for different scenarios. Plant Sci 282: 14–22
Google Scholar: Author Only Title Only Author and Title

Reynolds M, Langridge P (2016) Physiological breeding. Curr Opin Plant Biol 31: 162–171
Google Scholar: Author Only Title Only Author and Title

Ritter N, Ruth M (1997) The GeoTIFF data interchange standard for raster geographic images. Int J Remote Sens 18: 1637–1647

Google Scholar: Author Only Title Only Author and Title

Roitsch T, Cabrera-Bosquet L, Fournier A, Ghamkhar K, Jiménez-Berni J, Pinto F, Ober ES (2019) Review: New sensors and data-driven approaches-A path to next generation phenomics. Plant Sci 282: 2–10
Google Scholar: Author Only Title Only Author and Title

Roussel JR, Auty D, Coops NC, Tompalski P, Goodbody TRH, Meador AS, Bourdon JF, de Boissieu F, Achim A (2020) lidR: An R package for analysis of Airborne Laser Scanning (ALS) data. Remote Sens Environ 251: 112061
Google Scholar: Author Only Title Only Author and Title

Roy J, Tardieu F, Tixier-Boichard M, Schurr U (2017) European infrastructures for sustainable agriculture. Nat Plants 3: 756–758
Google Scholar: Author Only Title Only Author and Title

Sadras VO, Richards RA (2014) Improvement of crop yield in dry environments: Benchmarks, levels of organisation and the role of nitrogen. J Exp Bot 65: 1981–1995
Google Scholar: Author Only Title Only Author and Title

Sadras VO, Slafer GA (2012) Environmental modulation of yield components in cereals: Heritabilities reveal a hierarchy of phenotypic plasticities. F Crop Res 127: 215–224
Google Scholar: Author Only Title Only Author and Title

Sauvola J, Pietikäinen M (2000) Adaptive document image binarization. Pattern Recognit 33: 225–236
Google Scholar: Author Only Title Only Author and Title

Scharr H, Dee H, French AP, Tsaftaris SA (2016) Special issue on computer vision and image analysis in plant phenotyping. Mach Vis Appl 27: 607–609
Google Scholar: Author Only Title Only Author and Title

Shearman VJ, Scott RK, Foulkes MJ (2005) Crop Physiology and Metabolism. Physiological Processes Associated with Wheat Yield Progress in the UK. Crop Sci 185: 175–185
Google Scholar: Author Only Title Only Author and Title

Singh TR, Roy S, Singh OI, Sinam T, Singh KM (2012) A New Local Adaptive Thresholding Technique in Binarization. Int J Comput Sci Issues 8: 271–277
Google Scholar: Author Only Title Only Author and Title

Stovall AEL, Vorster AG, Anderson RS, Evangelista PH, Shugart HH (2017) Non-destructive aboveground biomass estimation of coniferous trees using terrestrial LiDAR. Remote Sens Environ 200: 31–42
Google Scholar: Author Only Title Only Author and Title

Su Y, Guo Q, Jin S, Guan H, Sun X, Ma Q, Hu T, Wang R, Li Y (2020) The Development and Evaluation of a Backpack LiDAR System for Accurate and Efficient Forest Inventory. IEEE Geosci Remote Sens Lett 1–5
Google Scholar: Author Only Title Only Author and Title

Su Y, Wu F, Ao Z, Jin S, Qin F, Liu B, Pang S, Liu L, Guo Q (2019) Evaluating maize phenotype dynamics under drought stress using terrestrial lidar. Plant Methods 15: 1–16
Google Scholar: Author Only Title Only Author and Title

Summerfield M (2015) Rapid GUI Programming with Python and Qt: The Definitive Guide to PyQt Programming. Pearson, London, UK
Google Scholar: Author Only Title Only Author and Title

Sun S, Li C, Paterson AH, Jiang Y, Xu R, Robertson JS, Snider JL, Chee PW (2018) In-field high throughput phenotyping and cotton plant growth analysis using LiDAR. Front Plant Sci 9: 1–17
Google Scholar: Author Only Title Only Author and Title

Susan S, Hanmandlu M (2013) A non-extensive entropy feature and its application to texture classification. Neurocomputing 120: 214–225
Google Scholar: Author Only Title Only Author and Title

Swarbreck SM, Wang M, Wang Y, Kindred D, Sylvester-Bradley R, Shi W, Varinderpal-Singh, Bentley AR, Griffiths H (2019) A Roadmap for Lowering Crop Nitrogen Requirement. Trends Plant Sci 24: 892–904
Google Scholar: Author Only Title Only Author and Title

Sylvester-Bradley R, Kindred DR (2009) Analysing nitrogen responses of cereals to prioritize routes to the improvement of nitrogen use efficiency. J Exp Bot 60: 1939–1951
Google Scholar: Author Only Title Only Author and Title

Tardieu F, Cabrera-Bosquet L, Pridmore T, Bennett M (2017) Plant Phenomics, From Sensors to Knowledge. Curr Biol 27: R770–R783
Google Scholar: Author Only Title Only Author and Title

Truong-Hong L, Laefer DF, Hinks T, Carr H (2013) Combining an angle criterion with voxelization and the flying voxel method in reconstructing building models from LiDAR data. Comput Civ Infrastruct Eng 28: 112–129
Google Scholar: Author Only Title Only Author and Title

Ubbens J, Cieslak M, Prusinkiewicz P, Stavness I (2018) The use of plant models in deep learning: An application to leaf counting in rosette plants. Plant Methods 14: 1–10

Google Scholar: Author Only Title Only Author and Title

UN Food & Agriculture Organization (2009) How to Feed the World in 2050. In FAO, ed, Proc. High-Level Expert Forum How to Feed World 2050. UN FAO, Rome, p 733

Google Scholar: Author Only Title Only Author and Title

Vadez V, Kholová J, Hummel G, Zhokhavets U, Gupta SK, Hash CT (2015) LeasyScan: A novel concept combining 3D imaging and lysimetry for high-throughput phenotyping of traits controlling plant water budget. J Exp Bot 66: 5581–5593

Google Scholar: Author Only Title Only Author and Title

Valluru R, Reynolds MP, Davies WJ, Sukumaran S (2017) Phenotypic and genome-wide association analysis of spike ethylene in diverse wheat genotypes under heat stress. New Phytol 214: 271–283

Google Scholar: Author Only Title Only Author and Title

Virlet N, Sabermanesh K, Sadeghi-Tehran P, Hawkesford MJ, Sabermanesh P, Sadeghitehran K, Hawkesford MJ, Sabermanesh K, Sadeghi-Tehran P, Hawkesford MJ (2017) Field Scanalyzer: An automated robotic field phenotyping platform for detailed crop monitoring. Funct Plant Biol 44: 143–153

Google Scholar: Author Only Title Only Author and Title

Virtanen P, Gommers R, Oliphant TE, Haberland M, Reddy T, Cournapeau D, Burovski E, Peterson P, Weckesser W, Bright J, et al (2020) SciPy 1.0: fundamental algorithms for scientific computing in Python. Nat Methods 17: 261–272

Google Scholar: Author Only Title Only Author and Title

Van Der Walt S, Colbert SC, Varoquaux G (2011) The NumPy array: A structure for efficient numerical computation. Comput Sci Eng 13: 22–30

Google Scholar: Author Only Title Only Author and Title

van der Walt S, Schönberger JL, Nunez-Iglesias J, Boulogne F, Warner JD, Yager N, Gouillart E, Yu T (2014) Scikit-image: image processing in Python. PeerJ 2: 1–18

Google Scholar: Author Only Title Only Author and Title

Walter JDC, Edwards J, McDonald G, Kuchel H (2019) Estimating Biomass and Canopy Height With LiDAR for Field Crop Breeding. Front Plant Sci. doi: 10.3389/fpls.2019.01145

Google Scholar: Author Only Title Only Author and Title

Wang C, Nie S, Xi X, Luo S, Sun X (2017) Estimating the biomass of maize with hyperspectral and LiDAR data. Remote Sens 9: 1–12

Google Scholar: Author Only Title Only Author and Title

Ward B, Brien C, Oakey H, Pearson A, Negrão S, Schilling RK, Taylor J, Jarvis D, Timmins A, Roy SJ, et al (2019) High-throughput 3D modelling to dissect the genetic control of leaf elongation in barley (Hordeum vulgare). Plant J 98: 555–570

Google Scholar: Author Only Title Only Author and Title

Wu D, Guo Z, Ye J, Feng H, Liu J, Chen G, Zheng J, Yan D, Yang X, Xiong X, et al (2019) Combining high-throughput micro-CT-RGB phenotyping and genome-wide association study to dissect the genetic architecture of tiller growth in rice. J Exp Bot 70: 545–561

Google Scholar: Author Only Title Only Author and Title

Yang W, Feng H, Zhang X, Zhang J, Doonan JH, Batchelor WD, Xiong L, Yan J (2020) Crop Phenomics and High-Throughput Phenotyping: Past Decades, Current Challenges, and Future Perspectives. Mol Plant 13: 187–214

Google Scholar: Author Only Title Only Author and Title

Zadocks JC, CHANG TT, KONZAK CF (1974) A decimal code for the growth stages of cereals. Weed Res 14: 415–421

Google Scholar: Author Only Title Only Author and Title

Zhang H, Li Y, Zhu JK (2018) Developing naturally stress-resistant crops for a sustainable agriculture. Nat Plants 4: 989–996

Google Scholar: Author Only Title Only Author and Title

Zhao C, Zhang Y, Du J, Guo X, Wen W, Gu S, Wang J, Fan J (2019) Crop phenomics: Current status and perspectives. Front Plant Sci. doi: 10.3389/fpls.2019.00714

Google Scholar: Author Only Title Only Author and Title

Zhao X, Guo Q, Su Y, Xue B (2016) Improved progressive TIN densification filtering algorithm for airborne LiDAR data in forested areas. ISPRS J Photogramm Remote Sens 117: 79–91

Google Scholar: Author Only Title Only Author and Title

Zhou J, Applegate C, Alonso AD, Reynolds D, Orford S, Mackiewicz M, Griffiths S, Penfield S, Pullen N (2017a) Leaf-GP: An open and automated software application for measuring growth phenotypes for arabidopsis and wheat. Plant Methods 13: 1–30

Google Scholar: Author Only Title Only Author and Title

Zhou J, Reynolds D, Websdale D, Le Cornu T, Gonzalez-Navarro O, Lister C, Orford S, Laycock S, Finlayson G, Stitt T, et al (2017b) CropQuant: An automated and scalable field phenotyping platform for crop monitoring and trait measurements to facilitate breeding and digital agriculture. bioRxiv 161547

Google Scholar: Author Only Title Only Author and Title

Zhou QY, Park J, Koltun V (2018) Open3D: A modern library for 3D data processing. arXiv 1–8
Google Scholar: Author Only Title Only Author and Title